Histone Lactylation Drives CD8 T Cell Metabolism and Function

Deblina Raychaudhuri[1†], Pratishtha Singh[1†], Mercedes Hennessey[1], Aminah J. Tannir[1], Bidisha Chakraborty[1], Seanu Meena Natarajan[1], Sangeeta Goswami[1,2,3]*

[1]Department of Immunology, The University of Texas MD Anderson Cancer Center, Houston, Texas. [2]Department of Genitourinary Medical Oncology, The University of Texas MD Anderson Cancer Center, Houston, Texas. [3]James P. Allison Institute, The University of Texas MD Anderson Cancer Center, Houston, Texas.

[†]Contributed equally

*Corresponding author. Email: sgoswami@mdanderson.org

Abstract

CD8 T cells undergo metabolic adaptations following activation to support cytotoxic functions against pathogen-infected cells and cancer cells. Upregulation of glycolysis, mitochondrial metabolism, and lactate generation mark CD8 T cell activation. Lactylation is a newly identified lactate-derived histone post-translational modification (hPTMs), however, the relevance of histone lactylation in the context of CD8 T cell activation and function is not known. Here, we show the enrichment of H3K18-lactylation (H3K18la) and H3K9-lactylation (H3K9la) in human and murine CD8 T cells, which act as transcription initiators of key genes regulating CD8 T cell-mediated cytotoxicity and effector function. Further, we delineate the distinct functional impacts of H3K18la and H3K9la on CD8 T cells- while H3K9la plays a critical role in naïve, activated as well as memory CD8 T cells, H3K18la acts as a major regulator in activated CD8 T cells. H3K9la is driven by both glycolysis and mitochondrial metabolic pathways whereas H3K18la is selectively derived from glycolysis, perpetuating a feed-forward loop. Of note, exogenous lactate does not regulate H3K18la or H3K9la in CD8 T cells, rather it reduces the enrichment of these marks in the promoter and enhancer regions of genes. Additionally, we demonstrate the link between H3K18la and mitochondrial fission and the association of H3K9la with mitochondrial fusion which contribute to the specific energy metabolism patterns observed in different T cell states. The distinct involvement of H3K18la and H3K9la in shaping mitochondrial dynamics highlights their role as potential epigenetic regulators of T cell metabolism. Overall, our data uncovers the crucial function of histone lactylation in governing the transcriptomic landscape regulating CD8 T cell function. Furthermore, it sheds light on the unique contributions of H3K18la and H3K9la in modulating CD8 T cell phenotype, intricately associated with their metabolic status.

Introduction

CD8 T cells (cytotoxic T cells) are critical for mounting an effective immune response against infections and tumors by eliminating pathogen-infected cells and cancer cells(*1-3*). A naïve CD8 T cell, following recognition of a target cell displaying cognate antigen-MHC-I complex, becomes activated and proliferates to generate effector CD8 T cells expressing cytotoxic molecules(*4*). T cells acquire metabolic adaptations to support their proliferation and effector functions. While resting T cells primarily depend on the mitochondrial metabolic pathways including tricarboxylic acid (TCA) cycle and oxidative phosphorylation (OXPHOS) to meet their energy requirements, activated T cells undergo a shift toward glycolysis(*5, 6*). Upregulation of glycolysis in activated CD8 T cells leads to increased generation of lactate(*7*). However, the effect of lactate on the epigenetic landscape and function of CD8 T cells is not known.

Lactylation of histone lysine residues is a newly discovered epigenetic modification(*8*). However, the relevance of histone lactylation in the context of CD8 T cell activation and function is not understood. In this study, we aimed to investigate the role of histone lactylation in regulation of CD8 T cells and delineate its functional implications. We demonstrated the enrichment of H3K18-lactylation (H3K18la) and H3K9-lactylation (H3K9la) following the activation of human and murine CD8 T cells. Additionally, we uncovered the role of H3K18la and H3K9la as transcription regulators in T cells, individually and in combination with other well-established active histone post-translational modifications (hPTMs). Importantly, inhibition of H3K18la and H3K9la resulted in decreased expression of T cell-specific genes leading to reduced cytotoxic activity of CD8 T cells, highlighting the importance of H3K18la and H3K9la in regulating CD8 T cell function.

While H3K9la plays an important role in naïve, activated and memory CD8 T cells, H3K18la acts as the major driver in activated CD8 T cells. Of note, contrary to previous studies which have shown exogenous lactate as a major regulator of H3K18la in macrophages, we showed that supraphysiological concentrations of exogenous lactate does not drive H3K18la and H3K9la in

CD8 T cells. Instead, H3K18la and H3K9la are primarily driven by endogenous metabolic pathways. Pharmacological inhibition of individual cellular metabolic pathways demonstrated that glycolysis drives both H3K18la and H3K9la while mitochondrial metabolic pathways selectively drive H3K9la. Inhibiting glycolysis with enolase and lactate dehydrogenase A (LDHA) inhibitors lowered both H3K18la and H3K9la levels. However, inhibiting ATP citrate lyase (ACLY), responsible for converting mitochondrial TCA cycle-derived citrate to acetyl-coA(*9*), only decreased H3K9la levels. Additionally, our data demonstrated that H3K9la is associated with mitochondrial fusion while H3K18la is linked with mitochondrial fission that contributes to the distinct energy metabolism pathways observed in different T cell states.

Overall, this study uncovers a fundamental role of histone lactylation in regulating the transcriptomic profile and function of CD8 T cells and provides insight into the distinct role of H3K18la and H3K9la in modulating CD8 T cell phenotype intricately linked to their metabolic state.

Results

T cell activation drives histone lactylation

To investigate the relevance of H3K18la and H3K9la in human peripheral CD8 T cells, we assessed the pattern of histone lactylation in naïve and effector CD8 T cells. We stimulated human CD8 T cells isolated from peripheral blood mononuclear cells (PBMCs) with anti-CD3 plus anti-CD28. Flow cytometry analysis revealed an increase in H3K18la and H3K9la in CD8 T cells in activated CD8 T cells compared to naïve CD8 T cells (Fig. 1a). Notably, Gzmb+CD69+ activated CD8 T cells exhibited higher levels of H3K18la and H3K9la compared to Gzmb-CD69- CD8 T cells (Extended Data Fig. 1a) supporting a direct association between T cell activation and histone lactylation.

Similarly, anti-CD3 plus anti-CD28 mediated activation of murine splenocytes enhanced H3K18la and H3K9la in CD8 T cells (Fig. 1b, Extended Data Fig. 1b), mirroring the findings from the human study. Of note, we observed increased production of lactate following T cell activation (Extended Data Fig. 1c).

Further, to interrogate the impact of antigen-specific CD8 T cell stimulation on H3K18la and H3K9la, we used CD8 T cells isolated from pmel-1 mice, a model widely used for studying antigen-specific T cell responses(*10*). Upon stimulation with the cognate GP100 antigen, we observed a robust increase in H3K18la and H3K9la levels in pmel CD8 T cells especially in Gzmb+Tbet+ CD8 T cells, while stimulation with the non-cognate lymphocytic choriomeningitis virus (LCMV) peptide failed to induce significant alterations in H3K18la and H3K9la which demonstrated the antigen-specificity of TCR signaling driven changes in H3K18la and H3K9la in CD8 T cells (Fig. 1c, Extended Data Fig. 1d). Next, to establish a causal relationship between T cell activation and H3K18la and H3K9la, we used a murine *Bhlhe40* knockout model (Bhlhe40 KO) that harbors defects in T cell activation(*11, 12*). Notably, compared to controls, *Bhlhe40* KO CD8 T cells exhibited significantly reduced levels of H3K18la and H3K9la following anti-CD3 plus anti-CD28 stimulation (Extended Data Fig. 1d), highlighting the impact of impaired T cell activation on H3K18la and H3K9la in CD8 T cells.

Next, to determine the in-vivo relevance of H3K18la and H3K9la in CD8 T cells, we used the OT-I murine model which harbors CD8 T cells bearing T cell receptor (TCR)s specific for the ova-antigen(*13*). We injected MB49 tumor cells engineered to express the ova peptide (MB49-ova) into the OT-I mice. We noted attenuated tumor growth of MB49-ova tumors compared to control (Fig. 1d). Further, analyses of flow cytometry data demonstrated higher H3K18la and H3K9la levels in IFNγ+ CD8 T cells within the tumor-draining lymph nodes of mice bearing MB49-ova tumors compared to control MB49 tumors (Fig. 1e, Extended Data Fig. 2a, b). Next, we aimed to elucidate the implications of H3K18la and H3K9la in the context of immune checkpoint therapy,

a potent inducer of T cell mediated anti-tumor responses(*14, 15*). Similar to previous data, we noted reduction in tumor sizes (Fig.1f) and increase in IFNγ+ intratumoral CD8 T cells in MB49 tumor-bearing mice treated with a combination of anti-PD-1 and anti-CTLA-4 compared to the control-MB49 tumor-bearing mice (Extended Data Fig. 2c). Importantly, we noted a substantial enhancement of H3K18la and H3K9la in intratumoral CD8 T cells from mice treated with the anti-PD-1 plus anti-CTLA-4 therapy (Fig.1g, Extended data Fig. 2d) which underscores the critical link between T cell activation and the dynamic regulation of histone lactylation. Cumulatively, our data demonstrate that CD8 T cell activation which results in the generation of lactate in CD8 T cells, results in the increase in H3K18la and H3K9la.

Histone lactylation regulate transcription initiation in CD8 T cells

To elucidate the role of H3K18la and H3K9la in the transcriptional regulation of CD8 T cells, we performed chromatin immunoprecipitation sequencing (ChIP-seq) using naïve and activated CD8 T cells. ChromHMM analysis(*16*) of the ChIP-seq data allowed us to classify the genomic regions into 7 distinct chromatin states based on specific combinations of histone modifications including trimethylation of histone H3 lysine 4 trimethylation (H3K4me3), histone H3 lysine 9 acetylation (H3K9ac), histone H3 lysine 27 acetylation (H3K27ac), histone H3 lysine 79 dimethylation (H3K79me2), histone H3 lysine 36 trimethylation (H3K36me3), histone H3 lysine 27 trimethylation (H3K27me3), H3K9la,H3K18la and RNA polymerase II (RNApol II) (Fig. 2a-c). H3K4me3 and H3K9ac are well-established epigenetic marks associated with transcription initiation and H3K27ac marks active enhancer regions(*17, 18*). H3K79me2 and H3K36me3 are associated with actively transcribed gene bodies while H3K27me3 is a mark of transcription repression(*17, 18*). We found that chromatin regions enriched with H3K18la or H3K9la marks displayed a pattern of active transcription-associated chromatin state characterized by the enrichment of other transcription initiation marks including H3K4me3, H3K9ac, and H3K27ac (Fig. 2a). Further, both

H3K18la and H3K9la marks exhibited significant enrichment in chromatin regions proximal to transcription start site (TSS) regions and CpG islands indicating their involvement in the regulation of transcription initiation and gene expression (Fig. 2a-c). Next, to delineate the relationship of H3K18la and H3K9la with the other hPTMs in T cells, we investigated the correlation of H3K18la and H3K9la with these PTMs. The correlation matrices revealed a distinct pattern of positive correlations between lactylation marks (H3K18la and H3K9la) and other marks associated with active transcription initiation including H3K4me3 and H3K9ac in promoter regions (Fig. 2d). Additionally, lactylation marks showed positive correlations with H3K27ac which marks active enhancer and promoter regions (Fig. 2d). We also observed positive correlations between lactylation marks and H3K79me2 and H3K36me3, which mark actively transcribed gene bodies (Fig. 2d). Importantly, we noted similar correlations in proximal and distal enhancer-like sequence bearing regions (pELS and dELS) but not in intergenic regions (Extended Data Fig. 3a-c). These findings indicate a potential role of histone lactylation marks in promoting active gene expression and transcriptional regulation in CD8 T cells.

Next, to gain a more comprehensive understanding of the dynamic alterations of histone modifications during the transition from the naive to activated state of CD8 T cells, we compared the PTM enrichment in the promoter, proximal enhancer, and distal enhancer regions in naïve and activated CD8 T cells. We noted enrichment of H3K9la, H3K4me3 and H3K9ac in the promoter regions in the naïve T cell state which increased following T cell activation along with increased RNApol II occupancy in the promoter regions (Fig. 2e, Extended Data Fig. 3d). Importantly, H3K18la which showed minimal enrichment in the naïve state, showed substantial enrichment in the promoter regions of genes following T cell activation (Fig. 2e). While H3K27ac is traditionally linked to active enhancers, we also noted enrichment of H3K18la and H3K9la marks in proximal enhancer region (pELS) of genes in activated CD8 T cells, consistent with RNApol II binding (Extended Data Fig. 4). This indicates that H3K18la and H3K9la play a dual

role, not only marking active promoters but also actively participating in the regulation of enhancer regions. Notably, we observed a significant enrichment of H3K18la compared to other histone PTMs in the distal enhancer region with concurrent increase in RNApol II occupancy in the activated CD8 T cells (Extended Data Fig. 4). This highlights a critical role of H3K18la in promoting gene transcription through proximal as well as distal enhancer region.

To determine the functional implications of promoter and enhancer regions marked by H3K18la or H3K9la, we compared RNApol II occupancy of regions marked by unique lactylation peaks, regions marked by unique peaks of other active PTM peaks including H3K4me3 and H3K27ac, and regions marked by overlapping lactylation peaks and H3K4me3 or H3K27ac peaks. In activated CD8 T cells, we observed that gene promoters enriched with unique H3K9la peaks displayed notably higher RNApol II occupancy when compared to promoter regions marked solely by H3K4me3 peaks (Fig. 2f). Similarly, promoters enriched with unique H3K18la peaks exhibited significantly elevated RNApol II binding in comparison to promoter regions marked by exclusive H3K4me3 peaks (Fig. 2g). These findings suggest that in CD8 T cells, RNApol II binding to gene promoters carrying H3K9la and H3K18la marks is higher compared to promoter regions marked by H3K4me3 alone. Additionally, distal enhancer-like sequences bearing overlapping H3K9la and H3K27ac peaks or H3K18la and H3K27ac peaks demonstrated higher RNApol II occupancy compared with H3K27ac alone marked enhancer regions (Fig. 2h). This suggests a synergistic effect of H3K9la and H3K18la with H3K27ac in driving gene transcription through distal enhancers during T cell activation.

To further investigate the interactions of transcription factors (TFs) with H3K18la and H3K9la marked promoter regions, we conducted a comprehensive TF binding motif enrichment analysis using Hypergeometric Optimization of Motif EnRichment (HOMER)(*19*). Investigation of the top 5 most enriched TF binding motifs demonstrated that H3K18la marked promoter regions are enriched in Ets transcription factor binding motifs while H3K9la marked promoter regions are

enriched for zinc finger (ZF) transcription factor binding motifs, in activated CD8 T cells (Fig. 2i). It is noteworthy that both the ETS and ZF transcription factors have been extensively recognized for their pivotal roles in shaping CD8 T cell differentiation, homeostasis, and functional outcomes(*20-25*). Overall, our findings demonstrate a complex interplay of H3K18la and H3K9la marks with other histone PTMs and TFs in driving transcription in of CD8 T cells. Further, it also highlights a distinct pattern of TF binding motif enrichment in H3K18la and H3K9la marked promoter regions.

Distinct role of H3K9la and H3K18la in CD8 T cells

Based on our data that demonstrated H3K9la enrichment in both naive and activated states while H3K18la enrichment was specifically noted in activated CD8 T cells (Fig. 2e), we investigated the differential enrichment of H3K18la and H3K9la across specific gene loci within naïve and activated states. In naive CD8 T cells, we observed enrichment of H3K9la in multiple T cell-associated genes including genes involved in maintaining T cell quiescence such as *Bach2, Foxo1, Klf2* (Fig. 3a), whereas in activated CD8 T cells effector genes including *Gzmm, Gzmk, Gzme, Prf1, Icos, Bhlhe40, Fasl,* and *Pdcd1* displayed distinct enrichment of H3K18la marks (Fig. 3b). To further delineate the functional impact of H3K18la and H3K9la in memory CD8 T cells, we generated memory CD8 T cells through prolonged IL-15 stimulation of activated T cells(*26, 27*). Comparative H3K18la and H3K9la profiling in memory CD8 T cells revealed significant enrichment of H3K9la peaks in genes associated with T cell functions including *Sell, Ccr7,* and *Il7r*, similar to the pattern observed in naive T cells (Fig. 3c). Minimal enrichment of H3K18la was noted in the memory CD8 T cells (Fig. 3c).

Next, we performed Gene Set Enrichment Analyses (GSEA)(*28*) of differentially enriched H3K18la and H3K9la marked gene loci between naïve, activated, and memory states. Notably,

H3K18la marks correlated with heightened inflammatory response and Jak-Stat signaling pathways upon T cell activation (Fig. 3d, Extended Data Fig. 5a, b). H3K9la marks were associated with upregulated oxidative phosphorylation pathway along with downregulated TNFα signaling and cytokine-cytokine receptor interaction pathways in activated T cells compared to their naive counterparts (Fig. 3e, Extended Data Fig. 5c, d). GSEA also linked H3K9la marks to upregulated inflammatory response and fatty acid metabolism pathways in memory CD8 T cells (Fig. 3f, Extended Data Fig. 5e, f).

Additionally, our analysis revealed that in activated CD8 T cells H3K9la marks are enriched in genes involved in OXPHOS including *Ndufa12, Ndufb8,* and *Atp5a1* while H3K18la marks are enriched in genes associated with glycolysis including *Hk1, Pfkl, and Pfkp* indicating a role of H3K18la and H3K9la in regulating specific metabolic pathways in activated CD8 T cells (Fig. 3b). Next, we interrogated the unique and overlapping peaks of H3K18la and H3K9la marks and annotated the genes specifically associated with these distinct peaks. Consistent with the differential enrichment analysis, we found that unique H3K9la peaks are enriched in mitochondrial respiratory pathways, including oxidative phosphorylation, electron transport chain, and ATP synthesis in naive T cells (Fig. 3g). Conversely, unique H3K18la peaks showed enrichment in glucose metabolism pathways in activated CD8 T cells (Fig. 3h). These findings demonstrated that H3K9la plays a role in modulating mitochondrial metabolism in CD8 T cells while H3K18la is particularly involved in regulating the glucose metabolism during T cell activation. Importantly, we observed that H3K18la marks are enriched in the mitochondrial fission pathway in activated T cells, while H3K9la marks show prominence in the mitochondrial fusion pathway in naïve and memory T cells (Fig. 3g, h, Extended Data Fig. 5g). Further, we found that the promoter regions of *Fis1*, a gene responsible for mitochondrial fission(*29, 30*), exhibited enrichment of H3K18la in activated T cells, aligning with increased RNApol II presence (Fig. 3i). In contrast, *Opa1*, known for promoting mitochondrial fusion in memory T cells(*31*), displayed significant enrichment of

H3K9la corresponding to increased RNApol II levels in the memory state (Fig. 3i). This suggests that H3K18la possibly plays a crucial role in regulating mitochondrial fission during T cell activation while H3K9la plays a pivotal role in governing mitochondrial fusion during the formation of memory T cells. These findings highlight that H3K18la and H3K9la are central players in dictating mitochondrial dynamics in T cells, influencing the critical processes of fission and fusion that contribute to the distinct energy metabolism pathways observed in different T cell states(*31-33*). Taken together, these findings reveal that while H3K18la enrichment is critical for effector functions of activated CD8 T cells, H3K9la plays a major role in the regulation of all 3 CD8 T cell subsets studied - naïve, activated, and memory. However, the functional contribution of H3K9la marks varies based on the differentiation stage of the CD8 T cell. While H3K9la regulates multiple facets of naïve and memory CD8 T cells including T cell homeostasis, effector functions, and metabolism, it has a more restricted role in activated T cells where it mostly regulates mitochondrial metabolism.

Endogenous metabolic pathways drive histone lactylation in CD8 T cells

Previous studies have reported that both endogenous glycolysis-derived lactate and exogenous lactate regulate histone lactylation in macrophages(*8, 34*). To determine the role of endogenous and exogenous lactate in the regulation of histone PTMs including H3K18la and H3K9la following T cell activation, we treated primary CD8 T cells with LDHA inhibitor which reduces endogenous glycolysis-derived lactate accumulation following T cell activation. Additionally, we added sodium-L-lactate to the CD8 T cell cultures to examine the impact of exogenous lactate on H3K18la and H3K9la in CD8 T cells. LDHA inhibition resulted in the depletion of both H3K18la and H3K9la marks from promoter and enhancer chromatin regions in activated T cells indicating the role of endogenous glycolysis derived lactate as a source of histone lactylation in activated CD8 T cells (Fig. 4a, Extended Data Fig. 6). H3K27ac levels on the other hand, increased following LDHA

inhibitor treatment while H3K9ac demonstrated partial depletion (Extended Data Fig. 6). Further, administration of exogenous lactate increased H3K9ac and H3K27ac levels but it reduced H3K18la and H3K9la levels (Fig. 4a, Extended Data Fig. 6), possibly due to inhibitory effects on glycolysis(*35, 36*). Cumulatively, these findings demonstrated that in activated CD8 T cells, H3K18la and H3K9la are primarily influenced by endogenous sources of lactate as opposed to exogenous lactate.

We observed a notable decrease in H3K18la consistent with a reduction in RNApol II occupancy, specifically in the promoter regions of critical T cell activation genes including *Gzmb, Pdcd1* and *Ifngr1* (Fig. 4b, Extended Data Fig. 7a). qPCR-based gene expression studies further confirmed the reduction in the expression of these genes (Fig. 4c, Extended Data Fig. 7b), directly implicating H3K18la as a critical regulator of gene transcription in activated T cells. Next, we assessed the functional implications of H3K18la depletion by LDHA inhibitor on CD8 T cells. Flow cytometry demonstrated significant reduction in Granzyme B production in response to LDHA inhibitor (Fig. 4d, Extended data Fig. 7c). We also noted reduced accumulation of interferon-gamma, an effector cytokine produced by activated T cells, in culture supernatants following LDHA inhibition (Extended Data Fig. 7d). Importantly, treatment with LDHA inhibitor significantly reduced T cell-mediated killing of cognate antigen expressing cancer cells (Fig. 4e, Extended data Fig. 7e). Together, these findings demonstrated that LDHA inhibition-mediated depletion of H3K18la impairs T cell function, highlighting the critical role of H3K18la in maintaining CD8 T cell effector function.

Additionally, LDHA inhibition caused significant depletion of H3K18la marks within the promoter region of *Pfkl*, a gene encoding a pivotal rate-limiting enzyme in glycolysis with concurrent loss of RNApol II (Fig. 4f). On the other hand, we noted depletion of H3K9la marks within the promoter region of *Pdha1*, the gene encoding the rate-limiting enzymes in pyruvate decarboxylation feeding the mitochondrial TCA cycle (Fig. 4g). Further, we noted depletion of H3K9la marks in the genes

regulating the metabolism of long-chain and short-chain fatty acids which are known to play an important role in the generation of memory CD8 T cells(*37-40*). Specifically, the promoter region of *Cpt1a, Hadh, Ffar3* and *Echs1* which encode enzymes regulating long-chain and short-chain FAO, showed lack of H3K9la enrichment following LDHA inhibitor treatment (Fig. 4h, Extended Data Fig. 7f). Overall, these findings establish the important roles of H3K18la and H3K9la in the T cell metabolic landscape, with H3K18la predominantly orchestrating glucose metabolism and H3K9la being a pivotal driver of mitochondrial metabolism.

Interestingly, while the LDHA inhibitor caused complete abrogation of H3K18la marks, H3K9la was only partially depleted (Fig. 4a), suggesting additional sources for H3K9la apart from glycolysis and LDHA-derived lactate. Additionally, we noted that H3K18la levels are notably elevated only in activated CD8 T cells, which are known for their high glycolytic activity. In contrast, the levels of H3K9la remain remarkably high in naïve or memory T cells which are dependent on mitochondrial respiration and where glycolysis is low. This led us to investigate the potential differences in the endogenous metabolic sources of H3K9la and H3K18la. To test this, we used inhibitors - POMHEX which targets enolase to block glycolysis-derived lactate generation and BMS-30341 which inhibits ACLY to hinder the generation of acetyl-coA from TCA cycle derived citrate(*41, 42*). Treatment with POMHEX reduced H3K9la and H3K18la levels in activated CD8 T cells (Fig. 4i, Extended Data Fig. 8a), mirroring our findings from the studies using the LDHA inhibitor and confirming the role of cellular glycolysis as a source of both H3K18la and H3K9la in activated CD8 T cells. Importantly, inhibition of ACLY with BMS-30341 caused a selective decrease in H3K9la levels in activated and memory CD8 T cells indicating mitochondrial metabolism as an additional source of H3K9la (Fig. 4j, Extended Data Fig. 8b, c).

Collectively, our findings demonstrated endogenous lactate rather than exogenous lactate as a major driver of H3K18la and H3K9la in CD8 T cells. While H3K18la is derived mainly from endogenous glycolytic pathways, H3K9la is derived from both glycolytic and mitochondrial

metabolic pathways. Overall, our data underscore the H3K18la and H3K9la mediated dynamic interplay between histone modifications and metabolic pathways to regulate CD8 T cell phenotype and function (Fig. 4k).

Discussion

This study uncovered the fundamental role of H3K18la and H3K9la in the regulation of CD8 T cell phenotype and function linked to their metabolic status. We noted significant enrichment of H3K18la and H3K9la in human and murine CD8 T cells, both in vitro and in vivo, underscoring the importance of histone lactylation as an essential epigenetic modification in CD8 T cells. We observed that H3K18la and H3K9la play a dual role, not only marking active promoters but also actively participating in the regulation of enhancer regions. Further, we provided insight into the role of H3K18la and H3K9la as key transcription regulators in CD8 T cells either individually or in conjunction with other well-established active histone PTMs. These findings underscored the complex interplay of histone lactylation with other epigenetic modifications in shaping the transcriptional landscape of CD8 T cells.

Pharmacological inhibition of individual cellular metabolic pathways allowed us to identify endogenous metabolic pathways, particularly glycolysis, as the primary driver of H3K18la and H3K9la in activated CD8 T cells. An important finding of our study was the attenuation of CD8 T cell effector function following LDHA inhibitor-mediated downregulation of H3K18la and H3K9la, establishing the significance of these lactylation marks as critical regulators of T cell function. Importantly, unlike H3K18la, H3K9la levels are also high in both naïve and memory CD8 T cells, which have low glycolytic activity. We found that mitochondrial metabolic pathways selectively drive H3K9la, indicating that H3K9la might be sourced from mitochondrial TCA cycle in addition to glycolysis whereas H3K18la is exclusively driven by glycolysis. Together, these data provided

important insights into the distinct metabolic pathways regulating H3K18la and H3K9la marks in CD8 T cells.

While specific endogenous metabolic pathways drive H3K18la and H3K9la linked to the phenotypic status of CD8 T cell subsets, H3K18la and H3K9la in turn, regulate key genes determining CD8 T cell state with H3K9la playing a major role in naïve, activated and memory CD8 T cells and H3K18la playing a major role in activated CD8 T cells. Importantly, we found that H3K9la is closely associated with mitochondrial fusion, a process crucial for the formation of larger, interconnected mitochondria observed in naive and memory T cells(*43, 44*). On the other hand, H3K18la enrichment was noted on critical genes regulating mitochondrial fission, promoting the fragmentation of mitochondria, which is particularly significant in activated CD8 T cells with high glycolytic activity(*43, 44*). The distinct involvement of H3K18la and H3K9la in shaping mitochondrial dynamics highlights their role as potential epigenetic regulators of T cell metabolism. By impacting mitochondrial fission and fusion, H3K18la and H3K9la likely influence the balance between glycolysis and OXPHOS, two fundamental metabolic pathways which in turn perpetuate a feed-forward loop by regulating H3K18la and H3K9la and CD8 T cell functionality.

Although glycolysis is a major source of energy in activated CD8 T cells, it has been demonstrated that the mitochondrial metabolic pathways are also upregulated following CD8 T cell activation(*45-47*). We noted enrichment of H3K9la in genes encoding rate-limiting enzymes of TCA cycle in activated CD8 T cells. Importantly, LDHA inhibition resulted in the loss of H3K9la enrichment in the promoter region of these genes regulating the TCA. A previous study had reported that deletion of LDHA reduced acetyl-CoA levels, and lowered binding of H3K9ac on *Ifnγ* enhancer, thus reducing its expression(*48*). However, the mechanism by which LDHA deficiency reduces acetyl-CoA levels, was not clearly delineated. Our findings demonstrating the lack of H3K9la enrichment in genes regulating TCA cycle and acetyl-CoA generation following LDHA inhibition provides a link between H3K9la and LDHA-mediated downregulation of H3K9ac.

Notably, contrary to previous data from macrophages(*8, 34*), our data indicated that exogenous lactate does not regulate H3K18la and H3K9la in activated T cells. Rather, we noted reduction of H3K18la and H3K9la in activated T cells following addition of sodium L-lactate. The counterintuitive effect of exogenous lactate on the reduction of H3K18la and H3K9la can be attributed to the recently reported inhibitory impact of L-lactate on glycolysis in T cells(*35*). Similar to the previous study(*8*), we treated CD8 T cells with supraphysiological concentrations (25mM) of exogenous lactate, which are found in certain diseased conditions such as in tumors(*49*). Therefore, monitoring the impact of physiological concentrations (2-3mM) of exogenous lactate on histone lactylation in CD8 T cells can be considered. Additionally, in our study, we have used sodium lactate- a pH-neutral form of lactate, instead of lactic acid to eliminate the non-specific impact of acidosis.

Overall, this study uncovers the fundamental role of histone lactylation in regulating the transcriptomic profile and function of CD8 T cells and provides insight into the distinct role of H3K18la and H3K9la in modulating CD8 T cell phenotype intricately linked to their metabolic state (Fig. 4k). It will be important to delineate how these epigenetic marks manifest in CD8 T cells from diverse diseased conditions including tumor and autoimmunity. Recent work has also demonstrated that H4K12la enrichment of glycolytic genes regulates gene expression in microglia in a preclinical model of Alzheimer's disease(*50*). It will be necessary to further explore the potential roles of H4K12la and other histone lactylation modifications in regulation of CD8 T cell homeostasis and functions. The identification of specific lactylation-driven metabolic pathways may offer exciting opportunities for therapeutic interventions aimed at modulating T cell function, with potential applications in cancer immunotherapy and other immune-related diseases. Modulating the activity of enzymes responsible for histone lactylation, or targeting specific lactylation marks, may offer novel therapeutic avenues for fine-tuning T cell responses in various disease contexts. While multiple OXPHOS inhibitors are under clinical development as cancer

therapeutics, it is important to understand the nuances of globally targeting these pathways considering the differential effects of these inhibitors on cancer cells and immune cells.

Methods

Ethics Statement. The research outlined in this study complies with all relevant ethical regulations. Animal experiments were approved by the Animal Resource Center at The University of Texas MD Anderson Cancer Center.

Human PBMC isolation and stimulation. Buffy coats derived from healthy human donors were collected from the blood bank. The blood was diluted 1:2 in PBS before 40ml of the diluted blood was gently layered on top of 10ml Ficoll Histopaque. The tubes were centrifuged at 1000Xg for 20 minutes at 25ºC in a swing bucket rotor. The white buffy coat layer containing the PBMCs present at the interphase was washed twice via centrifugation in 10ml of PBS. The pellet obtained was subjected to RBC lysis using ACK Lysis Buffer before being counted in a Vicell cell counter. 1.5-2X10^6 PBMCs/well were cultured in RPMI media supplemented with 10% FBS in 96 well flat-bottomed plates at 37ºC and 5% CO_2. For stimulation of T cells, the wells were coated with 2 µg/mL of anti-CD3 and 3 µg/mL of CD28 was added to the culture.

Flow cytometry. 2X10^6 cells were washed once in PBS containing 5% FBS (FACS buffer) by centrifugation at 200Xg for 5 minutes at 4 °C. Following the wash cells were incubated in blocking buffer containing bovine, murine, rat, hamster, rabbit serum and 25 µg/mL 2.4G2 antibody (Fc block) in PBS for 15 minutes on ice. Cells were then incubated for 30 minutes on ice in an antibody cocktail for surface staining (Supplementary Table 1). Following surface staining, cells were washed twice in FACS buffer before being subjected to fixation and permeabilization for 45 minutes on ice. After a wash with 1X permeabilization buffer, cells intracellular staining was

performed by incubating the cells for 20 minutes in a cocktail of antibodies (Supplementary Table X) at room temperature. Then the cells were washed twice in FACS buffer, fixed in 1% paraformaldehyde and acquired on a BD LSRFortessa flow cytometer.

Mice. 5–7-weeks old C57BL/6 mice, Bhlhe40 KO, pmel-I and OT-I mice were used in this study. Age and sex matched mice were used for experiments. Mice were housed at the Animal Resource Center, University of Texas MD Anderson Cancer Center where they were maintained in specific pathogen-free conditions, 20-25°C, 30-70% humidity and on a 12hour light/12hour dark cycle. Animal protocols were approved by the Institutional Animal Care and Use Committee of the University of Texas MD Anderson Cancer Center.

Murine splenocyte isolation and stimulation. C57BL/6 mice, Bhlhe40-/-, pmel-I and OT-I mice were dissected, and spleens harvested. Spleens were washed in ice-cold PBS before being mushed using the plunger of 1ml syringe and passed through a 70µ strainer. The single cell suspension obtained was washed in PBS by centrifugation at 220Xg for 5 minutes at 4ºC and the cell pellet was subjected to RBC lysis using ACK Lysis Buffer before being counted in a Vicell cell counter. 1.5-2 $X10^6$ splenocytes/well were cultured in RPMI media supplemented with 10% FBS in 96 well flat-bottomed plates at 37ºC and 5% CO_2. For stimulation of T cells, the wells were coated with 3 µg/mL of anti-CD3 and 2 µg/mL of CD28 was added to the culture. For specific experiments, splenocytes were stimulated with 1 µg/mL hGP100 peptide, 1 µg/mL LCMV peptide or 9.63 µg/mL SIINFEKL peptide as outlined in the figure legends. Further, to test the effect of pharmacological inhibition of specific metabolic pathways on H3K18la and H3K9la, stimulated T cells were treated with LDHA inhibitor, sodium L-lactate, POMHEX or BMS-30341 as indicated in the figure legends.

OT-1 tumor model. OT-I mice were subcutaneously injected in the right flank with $200X10^3$ MB49 control and MB49-ova cells resuspended in 100ul of PBS per mouse. On Day 10 following injection, mice were sacrificed and the tumor draining lymph nodes were isolated, mushed and a single-cell suspension was prepared as described above, for flow cytometry staining and acquisition.

Anti-CTLA-4 and anti-PD-1 treatment regimen. MB49 tumor-bearing C57BL/6 received intraperitoneal injections of 200µg, 100µg and 100µg of α-PD1 as well as α-CTLA-4 on day 3, 6 and 9 post tumor inoculation. On Day 14 the tumors were harvested for the preparation of a single-cell suspension and staining for flow cytometry as described above.

Magnet Assisted Cell sorting (MACS). Murine splenocytes were resuspended in MACS buffer containing 1X PBS containing 2mM EDTA and 0.5% BSA on ice before CD8 antibody Biotin cocktail was added to each sample. The samples were resuspended well and incubated on ice for 15 minutes before anti-biotin microbeads were added, resuspended well, and incubated on ice for 20 minutes. To remove unbound antibody, samples were washed in excess MACS Buffer by centrifugation at 200Xg at 4ºC for 5 minutes. Next, the cell pellets were resuspended in MACS buffer, run through LS columns and washed by addition of excess MACS buffer to collect CD8 T cells. For isolation of naïve or effector CD8 T cells, the same procedure was repeated on CD8 T cells using CD44+ microbeads.

Extracellular lactate measurement assay. To quantify the concentration of L-lactate generated following T cell activation, CD8 T cells were isolated from the spleens of C57BL/6 mice and stimulated with anti-CD3 and anti-CD28 as described above. Following 24 hours of stimulation,

culture supernatants were collected and subjected to lactate quantification using the L-Lactate Assay Kit according to the manufacturer's instructions.

ChIP Sequencing. Cells of interest were subjected to ChIP using the MAGnify Chromatin Immunoprecipitation System according to the Manufacturer's protocol. Briefly, 37% formaldehyde was added to the samples, mixed thoroughly, and incubated at room temperature for 10 minutes. Next, 1.5 M glycine was added to the samples and incubated at room temperature for 5 minutes. Following the crosslinking step, the samples were washed in cold PBS three times by centrifugation at 200 g for 10 minutes at 4ºC. Next, the cell pellets were resuspended in lysis buffer and were sonicated to shear the DNA to 150-300 kb fragments. For each immunoprecipitation reaction 10µg of H3K18lac, H3K9lac, H3K4me3, H3K9ac, H3K27ac, H3K79me2, H3K36me3, H3K27me3, and RNA Pol II antibodies were used and the samples were incubated overnight with the antibodies at 4ºC. The following day, excess antibody was washed off and the target DNA was purified and eluted. The concentration of precipitated DNA was quantified using a Qubit and dsDNA HS Assay kit. 10µg of immunoprecipitated DNA per condition was sent for sequencing to the MD Anderson Cancer Center Advanced Technology Genomics Core where sequencing was performed using the NextSeq500 instrument.

ChIP Sequencing data analysis. The quality of CHIPseq FASTQ sequences generated as described above, were assessed using FastQC v0.11.9, followed by mapping by bowtie2 v2.3.5.1(*51*) with mouse reference genome mm10. The bam files obtained from mapping were further processed using SAMBLASTER v0.1.26(*52*) and SAMTOOLS v1.13(*53*), for duplicate removal, sorting and indexing. Further, SAMBAMBA v0.6.6(*54*) was used to normalize the bam files per read counts by performing random sampling. The genome wide annotation of aligned reads was performed using ChromHMM v1.24(*16*) which applies multivariate hidden Markov model (HMM) to assign states by modeling combinatorial presence and absence of each mark.

The reads were subjected to “BinarizeBam” followed by “LearnModel” using mm10 assembly study enrichment and functional annotation of each mark in 7-state model. The bigwig files were generated from aligned bam reads with “bamCoverage” function of deepTools v3.5.1(*55*) and used to visualize gene tracks with Integrative Genomics Viewer (IGV) v2.16.0(*56*).

The ChIP-seq signal enrichment over "Input control" background was identified using Model based analysis of ChIP-seq (MACS)2 v2.2.8(*57*). The peaks with significant p-values (< 0.05) were considered for further annotation with using CHIPseeker v1.30.3(*58*) and clusterProfiler(*59*) packages in R v4.0.2. The gene ontology enrichment was performed with “enrichGO” function from clusterProfiler and list of pathways enriched in each peak set was obtained. The bed files of candidate cis-regulatory elements for pELS and dELS were obtained from the SCREEN project of ENCODE(*60*) and overlapped with MACS2 peaks using “findOverlapsOfPeaks” function from ChIPpeakAnno v3.28.1(*61*) package to identify enhancer regions present in respective peak-sets.

The correlation matrices for promoter, pELS and dELS peak regions between different datasets were computed with “computeMatrix” and “plotCorrelations” function of deepTools to obtain the data in “tab” formats which was plotted with “corrplot” function in R. The distribution of promoters, pELS and dELS were summarized and plotted with “plotHeatmap” function of deepTools. The pairwise combinatorial analysis was performed by finding overlapped and unique peak regions for promoters, pELS and dELS with ChIPpeakAnno package followed by Reads Per Million (RPM) estimation using EdgeR v3.36.0(*62*). The command “findMotifs.pl” from Homer v4.11.1(*19*) was used to identify the motifs enriched in peak regions for different marks using mm10 genome as background.

The quantitative pairwise comparisons of different datasets were performed using MAnorm v1.1.4(*63*) using both peak (bed) and read (bam) coordinates for respective sample. The significant enrichment of target genes was estimated of the basis of M value which describes the

log2 fold change and plotted with ggplot2. Differential pathways enriched among datasets were identified using GSEA v4.2.3(*28*).

RNA Isolation and cDNA preparation for qPCR. Single cell suspension of mouse splenocytes were stimulated, treated, and sorted as described above. The cells were resuspended in TriZol reagent before one-fifth volume of chloroform was added to the samples. Following the addition of chloroform, the samples were mixed vigorously for 1-2 minutes and incubated at room temperature for 10 minutes. The samples were then centrifuged at 12,000Xg for 10 minutes at 4ºC. The top aqueous layer was collected, and equal volume of isopropanol was added before incubation at room temperature for 10 minutes. The samples were again centrifuged at 12000Xg for 10 minutes at 4ºC before a final wash by centrifugation in 75% ethanol. Finally, the pellets were air-dried and resuspended in nuclease-free water. RNA concentration was measured using a Nanodrop and 1ug of RNA was reverse transcribed into cDNA using the Superscript III cDNA kit. This cDNA was used to perform real time PCR in order to measure the expression of the genes of interest. The primer sequences used have been outlined in Supplementary Table 1.

Enzyme-linked immunosorbent assay (ELISA). 96-well binding plates were coated overnight at 4ºC with mouse IFN-G capture antibody, diluted 5:1000 in coating buffer containing $NaHCO_3$ and Na_2CO_3 in deionized water. Next day, the plates are washed three times with wash buffer containing PBS + 0.05% Tween-20 before the wells were blocked with 1X assay diluent for 1 hour at room temperature with gentle agitation. Following three more washes IFN-G standards and samples were added to the designated wells and incubated at room temperature for 2 hours with gentle agitation. Following incubation, the wells were washed three times and then 5:1000 diluted mouse IFN-G detection antibody was added to each of the wells before incubation for 1 hour at room temperature. Following three more washes, 1:1000 Avidin-HRP solution was added to each

well and incubated at room temperature for 30 minutes. For the final step, the wells were soaked in wash buffer for 30 seconds for a total of four washes before TMB substrate solution was added and incubated in the dark until color development. Reactions were then stopped by the addition of Stop Solution to each well and the optical density values were read on a microplate spectrophotometer, at 450nm. The standard curve was prepared using linear regression based on the standard absorbance values of known concentrations. This allowed for proper quantification of the concentration of IFN-G present in the supernatants of the samples.

T cell cytotoxicity assay. Single-cell suspension was prepared from spleens were harvested from OT-I mice as described above. Splenocytes were either left unstimulated or stimulated with the SIINFEKL peptide for 48 hours in the presence or absence of 15µM LDHA inhibitor. MB49-ova cancer cells were also seeded in 24 well plates. Following stimulation of the splenocytes for 48 hours, CD8 T cells were sorted from each treatment condition using magnet-assisted cell sorting, counted and co-cultured with the MB49-ova cancer cells at a ratio of 4:1. Following 24 hours of co-culture, the cells were harvested and stained with an antibody cocktail containing CD45+ AF532, CD3e FITC, CD8a BV711, and annexin PB diluted in 1X Annexin Binding Buffer at room temperature for 15 minutes. The stained cells were then washed with 1X Annexin Binding Buffer and acquired in a BD LSRFortessa flow cytometer. FlowJo v10 was used for analysis of the flow cytometry data.

Statistics & Reproducibility. R v4.0.2 and GraphPad Prism software v9 was used for the statistical analyses. The specific statistical tests used have been indicated in the respective figure legends.

Code availability. The ChIP-seq analyses presented in the manuscript has been performed with open-source algorithms as described in the Methods section. Further details will be made available by authors upon request.

Acknowledgments

This research is supported by the MD Anderson Physician Scientist Award (S.G), Khalifa Physician Scientist Award (S.G), Andrew Sabin Family Foundation Fellows Award (S.G) and Clinic and Laboratory Integration Program Award (S.G). We acknowledge the UT MD Anderson Center ATGC Core (grant CA016672) for the sequencing studies. Dr. Goswami is a member of the James P. Allison Institute.

Author Contributions Statement

D.R and P.S designed and performed the experiments, analyzed data and wrote the manuscript. M.H performed experiments and wrote the manuscript. A.J.T, B.C and S.M.N helped with the murine experiments. S.G. developed the project, designed the experiments, analyzed data, wrote the manuscript and acquired funding.

Competing Interests Statement

The authors declare no competing interests.

Figure legends

Fig. 1: T cell activation drives histone lactylation. **a**, Representative histograms and box-and-whisker plots demonstrating H3K18la and H3K9la levels (median fluorescence intensity- MFI) in human CD8 T cells following indicated hours of anti-CD3 plus anti-CD28 stimulation. N=5 human donors. Two-tailed Student's t-test was performed. Whiskers represent minimum-maximum values. **b,** Representative histograms and box-and-whisker plots showing H3K18la and H3K9la

levels in murine CD8 T cells following indicated hours of CD3/CD28 stimulation. N= 3 female mice. Two-tailed Student's t-test was performed. Whiskers represent minimum-maximum values. **c,** Representative histograms and box-and-whisker plots depicting H3K18la and H3K9la levels in pmel mice-derived CD8 T cells stimulated with the cognate gp100 peptide or the control LCMV peptide. N= 3 female mice. Two-tailed Student's t-test was performed. Whiskers represent minimum-maximum values. **d**, Box-and-whisker plots demonstrating the weights of MB49 tumors and MB49-ova tumors derived from OT-I mice. N=9 female mice bearing control MB49 tumors and 8 female mice bearing MB49-ova tumors. One-tailed Student's t-test was performed. Whiskers represent minimum-maximum values. **e**, Box-and-whisker plots demonstrating H3K18la and H3K9la levels in TDLN-derived CD8 T cells from MB49 and MB49ova tumor bearing mice. N=9 female mice bearing MB49 tumors and 8 female mice bearing MB49-ova tumors. Two-tailed Student's t-test was performed. Whiskers represent minimum-maximum values. **f**, Box-and-whisker plots displaying the weights of MB49 tumors derived from control C57BL/6 mice and mice treated with a combination of anti-PD-1 and anti-CTLA4. N= 6 untreated female mice and 4 combination therapy treated mice. Two-tailed Student's t-test was performed. Whiskers represent minimum-maximum values. **g**, Box-and-whisker plots depicting H3K18la and H3K9la levels in MB49 tumor-derived CD8 T cells from control and combination therapy treated mice. N= 6 untreated female mice and 4 combination therapy treated mice. Two-tailed Student's t-test was performed. Whiskers represent minimum-maximum values.

Fig. 2: Histone lactylation regulates transcription initiation in CD8 T cells. **a**, Heatmap depicting emission parameters, generated from ChromHMM analysis. Each row corresponds to a specific chromatin state and each column corresponds to a specific epigenetic mark in naive and activated murine CD8 T cells. **b**, Heatmap displaying the fold enrichment of different chromatin states in distinct genomic regions based on the indicated epigenetic marks in naïve and activated CD8 T cells. **c,** Heatmap demonstrating the fold enrichment of different chromatin states around

transcription start site (TSS) based on epigenetic marks shown in **a,** in naïve and activated CD8 T cells. The darker blue color corresponds to a greater probability of observing the mark in the state. **d**, Correlation matrix demonstrating Spearman's correlation coefficients (color intensities and the size of circles) among H3K18la and H3K9la sites and the other indicated epigenetic modifications at the promoter regions (±1 kb from the TSS). **e**, Heatmaps demonstrating the genomic occupancy of the indicated histone PTMs at gene promoter regions in murine naïve and activated CD8 T cells. **f,g,h,** Violin plots depicting normalized RNApol II binding (log2RPM) in promoter **(f,g)** and distal enhancer regions of activated CD8 T cells **(h).** Regions have been categorized based on the combination of indicated histone PTMs. Two-tailed Student's t-test was performed. **i**, Dotplots demonstrating the top 5 significantly enriched transcription factor binding motifs in H3K18la (top panel) and H3K9la (bottom panel) marked promoter regions of activated CD8 T cells.

Fig. 3: Distinct roles of H3K9la and H3K18la in CD8 T cells**. a,b,c,** Volcano plots representing genes harboring differentially enriched H3K18la and H3K9la marks in naïve **(a)**, activated **(b),** and memory **(c)** CD8 T cells. Volcano plots shows the log2 ratio of fold change (log2FC) plotted against the Absolute Confidence, -log10 adjusted p-value (-log10(p)). The p-value was derived from the Students' t-test using MAnorm. **d,e,f,** Plots representing GSEA pathways generated from genes with H3K18la enrichment in activated CD8 T cells compared to naïve CD8 T cells **(d)**, genes with H3K9la enrichment or depletion in activated CD8 T cells compared to naïve CD8 T cells **(e)** and genes with H3K9la enrichment in memory CD8 T cells compared to activated CD8 T cells **(f).** P values were calculated by permutation using the GSEA software. **g,h,** Dotplots representing cellular metabolic pathways obtained from GO enrichment analysis on gene sets bearing unique H3K9la peaks in naïve CD8 T cells **(g)** and unique H3K18la peaks in activated CD8 T cells **(h).** The p-values were calculated by hypergeometric test using ChIPpeakAnno. **i,**

Genome Browser view of H3K18la, H3K9la, and RNApol II peaks at the *Opa1* and *Fis1* gene promoter regions (TSS ± 1kb) in the indicated CD8 T cell subsets.

Fig. 4: Endogenous metabolic pathways drive histone lactylation in CD8 T cells**. a,** Heatmaps demonstrating the genomic occupancy of the indicated histone PTMs at TSS ± 1kb flanking TSSs in naïve, activated, 15 μM LDHA inhibitor treated (LDHA) and sodium-lactate treated (LA) CD8 T cells. **b,** Genome Browser view of H3K18la and RNApol II binding at the Granzyme B *(Gzmb)* gene promoter (TSS ±1kb) in naïve, activated and LDHA inhibitor treated (LDHAi) CD8 T cells. **c,** Barplot showing the relative expression of Granzyme B (Gzmb) in naïve, activated and LDHA inhibitor treated CD8 T cells normalized to the expression of β-actin as determined by quantitative PCR. **d,** Box-and-whisker plots showing the median fluorescence intensity (MFI) of Granzyme B (Gzmb) in naïve, activated and 15μM LDHA inhibitor treated CD8 T cells as determined by flow cytometry. N=4 biologically independent samples/group. Two-tailed Student's t-test was performed. Whiskers represent maximum-minimum values. **e,** (Left panel) Box and whisker plots representing the ratio of MB49-ova cancer cells: T cells following 24-hour co-culture of the cancer cells with unstimulated, SIINFEKL pre-stimulated and LDHA inhibitor treated OT-I CD8 T cells. (Right panel) Box and whisker plots representing the percentage of annexin-V positive MB49-ova cancer cells following 24-hour co-culture with unstimulated, SIINFEKL pre-stimulated and LDHA inhibitor treated OT-I CD8 T cells. N=3-5 biologically independent samples/group. Two-tailed Student's t-test was performed. Whiskers represent minimum to maximum values. **f-h**, Genome Browser view of H3K18la **(f)**, H3K9la **(g,h)** and RNApol II binding at the promoter regions (TSS ±1kb) of the indicated genes in naïve, activated and LDHA inhibitor treated (LDHAi) CD8 T cells. **i**, Box-and-whisker plots showing the median fluorescence intensity (MFI) of H3K18la (top panel) and H3K9la (bottom panel) in CD8 T cells treated as indicated, determined by flow cytometry. N=6 biologically independent samples/group. Two-tailed Student's t-test was performed. Whiskers represent maximum-minimum values. **j**, Box-and-whisker plot showing the median

fluorescence intensity (MFI) of H3K18la and H3K9la in CD8 T cells treated as indicated, determined by flow cytometry. 5μM of the ACLY inhibitor- BMS-303141 was used for this experiment. N=6 biologically independent samples/group. Two-tailed Student's t-test was performed. Whiskers represent maximum-minimum values. **k**, Graphical summary of the findings presented in this study depicting the role of histone lactylation in the regulation of gene transcription, metabolism and effector function in CD8 T cells.

Extended Data Figure legends

Extended Data Figure 1: a, Representative histograms and box-and-whisker plots demonstrating the differences in H3K18la and H3K9la levels between human Gzmb+CD69+ and Gzmb-CD69- CD8 T cells following 24 hours of anti-CD3 and anti-CD28 stimulation. N=6 human donors. Two-tailed Student's t-test was performed. Whiskers represent minimum-maximum values. **b**, Representative histograms and box-and-whisker plots showing H3K18la and H3K9la levels in murine Tbet+Ifng+ and Tbet-Ifng- CD8 T cells following 24 hours of anti-CD3 and anti-CD28 stimulation. N= 3 female mice. Two-tailed Student's t-test was performed. Whiskers represent minimum-maximum values. **c**, Box-and-whisker plot demonstrating the concentration of L-lactate in the culture supernatant of murine CD8 T cells treated for 24 hours as indicated. N= 3 female mice. One-tailed Student's t-test was performed. Whiskers represent minimum-maximum values. **d,** Representative histograms and box-and-whisker plots depicting H3K18la and H3K9la levels in pmel mice-derived Tbet+Gzmb+ and Tbet-Gzmb- CD8 T cells stimulated with the cognate gp100 peptide. N= 3 female mice. Two-tailed Student's t-test was performed. Whiskers represent minimum-maximum values. **e**, Representative histograms and box-and-whisker plots demonstrating H3K18la and H3K9la levels in CD8 T cells derived from control C57BL/6 mice and Bhlhe40KO mice following anti-CD3 and anti-CD28 stimulation for 48 hours.

N=6 female mice. Two-tailed Student's t-test was performed. Whiskers represent minimum-maximum values.

Extended Data Figure 2: a, Representative histograms showing H3K18la and H3K9la levels in IFNg+ CD8 T cells derived from the TDLNs of control and MB49-ova tumor bearing mice. **b**, Box-and-whisker plots demonstrating the percentage of IFNg+CD8 T cells in TDLNs of control and MB49-ova tumor bearing mice. N=5 female mice bearing control MB49 tumors and 7 female mice bearing MB49-ova tumors. **c**, Representative box-and-whisker plot depicting IFNgamma expression in intratumoral CD8 T cells derived from control and anti-PD1 plus anti-CTLA4 treated MB49 tumor bearing mice. N= 6 control female mice and 4 female mice treated with a combination of anti-PD1 and anti-CTLA4. Two-tailed Student's t-test was performed. Whiskers represent minimum-maximum values. **d**, Representative histograms demonstrating the expression of H3K18la and H3K9la in intratumoral CD8 T cells derived from control and anti-PD1 plus anti-CTLA4 treated MB49 tumor bearing mice.

Extended Data Figure 3: a-c, Correlation matrices showing the Spearman's correlation coefficients (color intensities and the size of circles) among H3K18la and H3K9la sites and the other indicated hPTMs at proximal enhancer-like sequences (pELS) (a), distal enhancer-like sequences (dELS) (b) and intergenic regions (c). **d**, Heatmap depicting the genomic occupancy of RNApol II at gene promoter regions in murine naïve and activated CD8 T cells.

Extended Data Figure 4: Heatmaps depicting the genomic occupancy of the indicated hPTMs and RNApol II at pELS and dELS in murine naïve and activated CD8 T cells.

Extended Data Figure 5: a, Volcano plot representing genes differentially enriched for H3K18la marks in naïve and activated murine CD8 T cells. Volcano Plot shows the log2 ratio of fold change (log2FC) plotted against the Absolute Confidence, -log10 adjusted p-value (-log10(p)). The p-value was derived from the Students' t-test using MAnorm. **b**, Genome Browser view comparing

H3K18la peaks at the indicated genes in naïve and activated CD8 T cells. **c**, Volcano plot depicting genes differentially enriched for H3K9la marks in naïve and activated murine CD8 T cells. Volcano Plot shows the log2 ratio of fold change (log2FC) plotted against the Absolute Confidence, -log10 adjusted p-value (-log10(p)). The p-value was derived from the Students' t-test using MAnorm. **d**, Genome Browser view comparing H3K9la peaks at the indicated genes in naïve and activated CD8 T cells. Plot representing GSEA pathway generated from genes with H3K9la depletion in naive CD8 T cells compared to activated CD8 T cells**.** P values were calculated by permutation using the GSEA software. **e, f,** Volcano plots representing genes differentially enriched for H3K9la (**e**) or H3K18la (**f**) marks in activated and memory murine CD8 T cells. Volcano Plots show the log2 ratio of fold change (log2FC) plotted against the Absolute Confidence, -log10 adjusted p-value (-log10(p)). The p-value was derived from one sample Students' *t*-test using MAnorm. **g**, Dotplot representing cellular metabolic pathways obtained from GO enrichment analysis on gene sets bearing unique H3K9la peaks in memory CD8 T cells**.** The p-value was calculated by hypergeometric test using ChIPpeakAnno.

Extended Data Figure 6: Heatmaps demonstrating the genomic occupancy of the indicated hPTMs at promoter, pELS and dELS in naïve, activated, LDHA inhibitor-treated (LDHAi), and sodium-lactate treated (LA) CD8 T cells.

Extended Data Figure 7: a, Genome Browser view comparing H3K18la and RNApol II peaks at the TSS ±1kb regions of the indicated genes in naïve, activated and 15μM LDHA treated (LDHAi) CD8 T cells. **b**, Barplots showing the relative expression of the indicated genes in naïve, activated and LDHA inhibitor treated CD8 T cells normalized to the expression of β-actin as determined by quantitative PCR. **c**, Representative histograms showing Granzyme B levels in naïve, activated and 15 μM LDHA treated murine CD8 T cells. **d**, Box-and-whisker plot demonstrating the concentration of interferon gamma in culture supernatants of naïve, activated and 15 μM LDHA treated murine CD8 T cells. N=3 female mice. Two-tailed Student's t-test was performed.

Whiskers represent maximum-minimum values. **e**, (Top panel) Representative pseudocolor plots demonstrating the percentage of MB49-ova cancer cells and OT-I CD8 T cells following 24-hour co-culture of the cancer cells with unstimulated, SIINFEKL pre-stimulated and 15µM LDHA inhibitor treated OT-I CD8 T cells. (Bottom panel) Representative pseudocolor plots depicting the percentage of annexin-V positive MB49-ova cancer cells following 24-hour co-culture with unstimulated, SIINFEKL pre-stimulated and 15 µM LDHA inhibitor treated OT-I CD8 T cells. **f,** Genome Browser view comparing H3K9la and RNApol II peaks at the TSS ±1kb regions of the indicated genes in naïve, activated and 15µM LDHA treated CD8 T cells.

Extended Data Figure 8: a,b, Representative histograms demonstrating H3K18la and H3K9la levels in murine CD8 T cells treated as indicated. **c**, Box-and-whisker plots showing the median fluorescence intensity of H3K18la and H3K9la in memory CD8 T cells treated with indicated concentrations of the ACLY inhibitor- BMS-303141, determined by flow cytometry. N=6 biologically independent samples/group. Two-tailed Student's t-test was performed. ns= non-significant. Whiskers represent maximum-minimum values.

References

1. P. Wong, E. G. Pamer, CD8 T cell responses to infectious pathogens. *Annu Rev Immunol* **21**, 29-70 (2003).
2. A. M. van der Leun, D. S. Thommen, T. N. Schumacher, CD8(+) T cell states in human cancer: insights from single-cell analysis. *Nat Rev Cancer* **20**, 218-232 (2020).
3. M. St Paul, P. S. Ohashi, The Roles of CD8(+) T Cell Subsets in Antitumor Immunity. *Trends Cell Biol* **30**, 695-704 (2020).
4. J. T. Harty, A. R. Tvinnereim, D. W. White, CD8+ T cell effector mechanisms in resistance to infection. *Annu Rev Immunol* **18**, 275-308 (2000).
5. R. I. K. Geltink, R. L. Kyle, E. L. Pearce, Unraveling the Complex Interplay Between T Cell Metabolism and Function. *Annu Rev Immunol* **36**, 461-488 (2018).
6. N. J. MacIver, R. D. Michalek, J. C. Rathmell, Metabolic regulation of T lymphocytes. *Annu Rev Immunol* **31**, 259-283 (2013).
7. J. T. Grist *et al.*, Extracellular Lactate: A Novel Measure of T Cell Proliferation. *J Immunol* **200**, 1220-1226 (2018).
8. D. Zhang *et al.*, Metabolic regulation of gene expression by histone lactylation. *Nature* **574**, 575-580 (2019).

9. M. Dominguez, B. Brune, D. Namgaladze, Exploring the Role of ATP-Citrate Lyase in the Immune System. *Front Immunol* **12**, 632526 (2021).
10. W. W. Overwijk *et al.*, Tumor regression and autoimmunity after reversal of a functionally tolerant state of self-reactive CD8+ T cells. *J Exp Med* **198**, 569-580 (2003).
11. A. J. Salmon *et al.*, BHLHE40 Regulates the T-Cell Effector Function Required for Tumor Microenvironment Remodeling and Immune Checkpoint Therapy Efficacy. *Cancer Immunol Res* **10**, 597-611 (2022).
12. C. Li *et al.*, The Transcription Factor Bhlhe40 Programs Mitochondrial Regulation of Resident CD8(+) T Cell Fitness and Functionality. *Immunity* **51**, 491-507 e497 (2019).
13. K. A. Hogquist *et al.*, T cell receptor antagonist peptides induce positive selection. *Cell* **76**, 17-27 (1994).
14. P. Sharma *et al.*, Immune checkpoint therapy-current perspectives and future directions. *Cell* **186**, 1652-1669 (2023).
15. P. Sharma *et al.*, The Next Decade of Immune Checkpoint Therapy. *Cancer Discov* **11**, 838-857 (2021).
16. J. Ernst, M. Kellis, Chromatin-state discovery and genome annotation with ChromHMM. *Nat Protoc* **12**, 2478-2492 (2017).
17. P. B. Talbert, S. Henikoff, The Yin and Yang of Histone Marks in Transcription. *Annu Rev Genomics Hum Genet* **22**, 147-170 (2021).
18. G. Millan-Zambrano, A. Burton, A. J. Bannister, R. Schneider, Histone post-translational modifications - cause and consequence of genome function. *Nat Rev Genet* **23**, 563-580 (2022).
19. S. Heinz *et al.*, Simple combinations of lineage-determining transcription factors prime cis-regulatory elements required for macrophage and B cell identities. *Mol Cell* **38**, 576-589 (2010).
20. N. Muthusamy, K. Barton, J. M. Leiden, Defective activation and survival of T cells lacking the Ets-1 transcription factor. *Nature* **377**, 639-642 (1995).
21. C. T. Luo *et al.*, Ets transcription factor GABP controls T cell homeostasis and immunity. *Nat Commun* **8**, 1062 (2017).
22. C. Y. Wang, B. Petryniak, C. B. Thompson, W. G. Kaelin, J. M. Leiden, Regulation of the Ets-related transcription factor Elf-1 by binding to the retinoblastoma protein. *Science* **260**, 1330-1335 (1993).
23. M. R. Smith-Raska *et al.*, The Transcription Factor Zfx Regulates Peripheral T Cell Self-Renewal and Proliferation. *Front Immunol* **9**, 1482 (2018).
24. D. M. Schauder *et al.*, E2A-regulated epigenetic landscape promotes memory CD8 T cell differentiation. *Proc Natl Acad Sci U S A* **118**, (2021).
25. T. Guan *et al.*, ZEB1, ZEB2, and the miR-200 family form a counterregulatory network to regulate CD8(+) T cell fates. *J Exp Med* **215**, 1153-1168 (2018).
26. K. Pilipow *et al.*, IL15 and T-cell Stemness in T-cell-Based Cancer Immunotherapy. *Cancer Res* **75**, 5187-5193 (2015).
27. M. J. Richer *et al.*, Inflammatory IL-15 is required for optimal memory T cell responses. *J Clin Invest* **125**, 3477-3490 (2015).
28. A. Subramanian *et al.*, Gene set enrichment analysis: a knowledge-based approach for interpreting genome-wide expression profiles. *Proc Natl Acad Sci U S A* **102**, 15545-15550 (2005).
29. R. Yu, S. B. Jin, U. Lendahl, M. Nister, J. Zhao, Human Fis1 regulates mitochondrial dynamics through inhibition of the fusion machinery. *EMBO J* **38**, (2019).
30. H. Kim *et al.*, Fine-tuning of Drp1/Fis1 availability by AKAP121/Siah2 regulates mitochondrial adaptation to hypoxia. *Mol Cell* **44**, 532-544 (2011).
31. M. D. Buck, D. O'Sullivan, E. L. Pearce, T cell metabolism drives immunity. *J Exp Med* **212**, 1345-1360 (2015).

32. A. S. Rambold, E. L. Pearce, Mitochondrial Dynamics at the Interface of Immune Cell Metabolism and Function. *Trends Immunol* **39**, 6-18 (2018).
33. L. Simula *et al.*, Drp1 Controls Effective T Cell Immune-Surveillance by Regulating T Cell Migration, Proliferation, and cMyc-Dependent Metabolic Reprogramming. *Cell Rep* **25**, 3059-3073 e3010 (2018).
34. R. A. Irizarry-Caro *et al.*, TLR signaling adapter BCAP regulates inflammatory to reparatory macrophage transition by promoting histone lactylation. *Proc Natl Acad Sci U S A* **117**, 30628-30638 (2020).
35. W. J. Quinn, 3rd *et al.*, Lactate Limits T Cell Proliferation via the NAD(H) Redox State. *Cell Rep* **33**, 108500 (2020).
36. X. Cai *et al.*, Lactate activates the mitochondrial electron transport chain independent of its metabolism. *bioRxiv*, (2023).
37. M. Luu *et al.*, Microbial short-chain fatty acids modulate CD8(+) T cell responses and improve adoptive immunotherapy for cancer. *Nat Commun* **12**, 4077 (2021).
38. A. Bachem *et al.*, Microbiota-Derived Short-Chain Fatty Acids Promote the Memory Potential of Antigen-Activated CD8(+) T Cells. *Immunity* **51**, 285-297 e285 (2019).
39. G. J. van der Windt *et al.*, Mitochondrial respiratory capacity is a critical regulator of CD8+ T cell memory development. *Immunity* **36**, 68-78 (2012).
40. D. O'Sullivan *et al.*, Memory CD8(+) T cells use cell-intrinsic lipolysis to support the metabolic programming necessary for development. *Immunity* **41**, 75-88 (2014).
41. Y. H. Lin *et al.*, An enolase inhibitor for the targeted treatment of ENO1-deleted cancers. *Nat Metab* **2**, 1413-1426 (2020).
42. Y. Zheng *et al.*, ATP citrate lyase inhibitor triggers endoplasmic reticulum stress to induce hepatocellular carcinoma cell apoptosis via p-eIF2alpha/ATF4/CHOP axis. *J Cell Mol Med* **25**, 1468-1479 (2021).
43. M. Lisci, G. M. Griffiths, Arming a killer: mitochondrial regulation of CD8(+) T cell cytotoxicity. *Trends Cell Biol* **33**, 138-147 (2023).
44. M. D. Buck *et al.*, Mitochondrial Dynamics Controls T Cell Fate through Metabolic Programming. *Cell* **166**, 63-76 (2016).
45. E. M. Steinert, K. Vasan, N. S. Chandel, Mitochondrial Metabolism Regulation of T Cell-Mediated Immunity. *Annu Rev Immunol* **39**, 395-416 (2021).
46. S. Dimeloe, A. V. Burgener, J. Grahlert, C. Hess, T-cell metabolism governing activation, proliferation and differentiation; a modular view. *Immunology* **150**, 35-44 (2017).
47. N. Ron-Harel, A. H. Sharpe, M. C. Haigis, Mitochondrial metabolism in T cell activation and senescence: a mini-review. *Gerontology* **61**, 131-138 (2015).
48. M. Peng *et al.*, Aerobic glycolysis promotes T helper 1 cell differentiation through an epigenetic mechanism. *Science* **354**, 481-484 (2016).
49. K. G. de la Cruz-Lopez, L. J. Castro-Munoz, D. O. Reyes-Hernandez, A. Garcia-Carranca, J. Manzo-Merino, Lactate in the Regulation of Tumor Microenvironment and Therapeutic Approaches. *Front Oncol* **9**, 1143 (2019).
50. R. Y. Pan *et al.*, Positive feedback regulation of microglial glucose metabolism by histone H4 lysine 12 lactylation in Alzheimer's disease. *Cell Metab* **34**, 634-648 e636 (2022).
51. B. Langmead, S. L. Salzberg, Fast gapped-read alignment with Bowtie 2. *Nat Methods* **9**, 357-359 (2012).
52. G. G. Faust, I. M. Hall, SAMBLASTER: fast duplicate marking and structural variant read extraction. *Bioinformatics* **30**, 2503-2505 (2014).
53. H. Li *et al.*, The Sequence Alignment/Map format and SAMtools. *Bioinformatics* **25**, 2078-2079 (2009).
54. A. Tarasov, A. J. Vilella, E. Cuppen, I. J. Nijman, P. Prins, Sambamba: fast processing of NGS alignment formats. *Bioinformatics* **31**, 2032-2034 (2015).

55. F. Ramirez *et al.*, deepTools2: a next generation web server for deep-sequencing data analysis. *Nucleic Acids Res* **44**, W160-165 (2016).
56. J. T. Robinson *et al.*, Integrative genomics viewer. *Nat Biotechnol* **29**, 24-26 (2011).
57. Y. Zhang *et al.*, Model-based analysis of ChIP-Seq (MACS). *Genome Biol* **9**, R137 (2008).
58. Q. Wang *et al.*, Exploring Epigenomic Datasets by ChIPseeker. *Curr Protoc* **2**, e585 (2022).
59. G. Yu, L. G. Wang, Y. Han, Q. Y. He, clusterProfiler: an R package for comparing biological themes among gene clusters. *OMICS* **16**, 284-287 (2012).
60. E. P. Consortium *et al.*, Expanded encyclopaedias of DNA elements in the human and mouse genomes. *Nature* **583**, 699-710 (2020).
61. L. J. Zhu *et al.*, ChIPpeakAnno: a Bioconductor package to annotate ChIP-seq and ChIP-chip data. *BMC Bioinformatics* **11**, 237 (2010).
62. M. D. Robinson, D. J. McCarthy, G. K. Smyth, edgeR: a Bioconductor package for differential expression analysis of digital gene expression data. *Bioinformatics* **26**, 139-140 (2010).
63. Z. Shao, Y. Zhang, G. C. Yuan, S. H. Orkin, D. J. Waxman, MAnorm: a robust model for quantitative comparison of ChIP-Seq data sets. *Genome Biol* **13**, R16 (2012).

Fig. 1

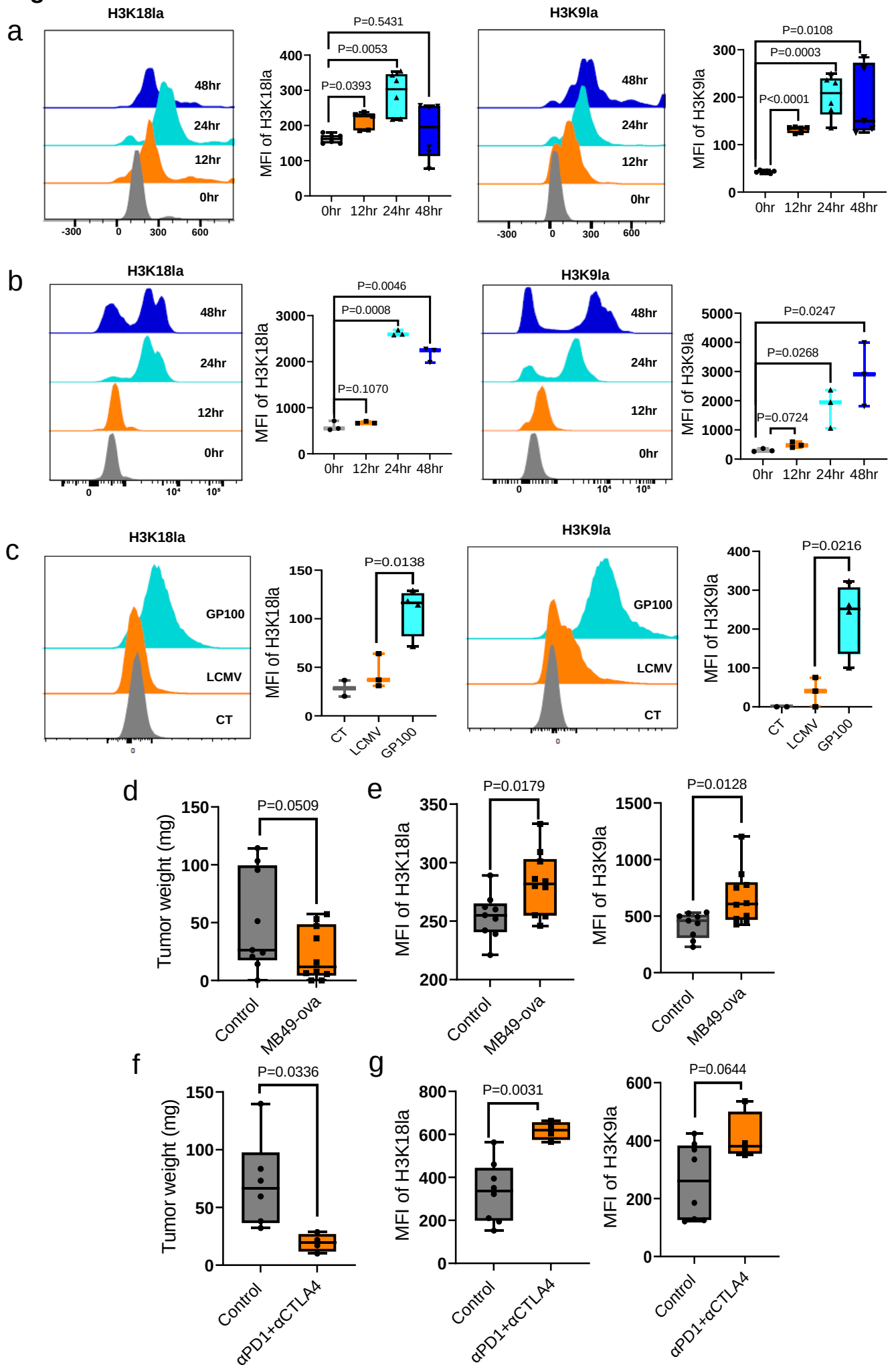
a
H3K18la
48hr
24hr
12hr
0hr
-300
0
300
600
P=0.5431
P=0.0053
P=0.0393
MFI of H3K18la
400
300
200
100
0
0hr 12hr 24hr 48hr
H3K9la
48hr
24hr
12hr
0hr
-300
0
300
600
P=0.0108
P=0.0003
P<0.0001
MFI of H3K9la
300
200
100
0
0hr 12hr 24hr 48hr
b
H3K18la
48hr
24hr
12hr
0hr
0
10⁴
10⁵
P=0.0046
P=0.0008
P=0.1070
MFI of H3K18la
3000
2000
1000
0
0hr 12hr 24hr 48hr
H3K9la
48hr
24hr
12hr
0hr
0
10⁴
10⁵
P=0.0247
P=0.0268
P=0.0724
MFI of H3K9la
5000
4000
3000
2000
1000
0
0hr 12hr 24hr 48hr
c
H3K18la
GP100
LCMV
CT
0
P=0.0138
MFI of H3K18la
150
100
50
0
CT LCMV GP100
H3K9la
GP100
LCMV
CT
0
P=0.0216
MFI of H3K9la
400
300
200
100
0
CT LCMV GP100
d
P=0.0509
Tumor weight (mg)
150
100
50
0
Control
MB49-ova
e
P=0.0179
MFI of H3K18la
350
300
250
200
Control
MB49-ova
P=0.0128
MFI of H3K9la
1500
1000
500
0
Control
MB49-ova
f
P=0.0336
Tumor weight (mg)
150
100
50
0
Control
αPD1+αCTLA4
g
P=0.0031
MFI of H3K18la
800
600
400
200
0
Control
αPD1+αCTLA4
P=0.0644
MFI of H3K9la
600
400
200
0
Control
αPD1+αCTLA4

Fig. 2

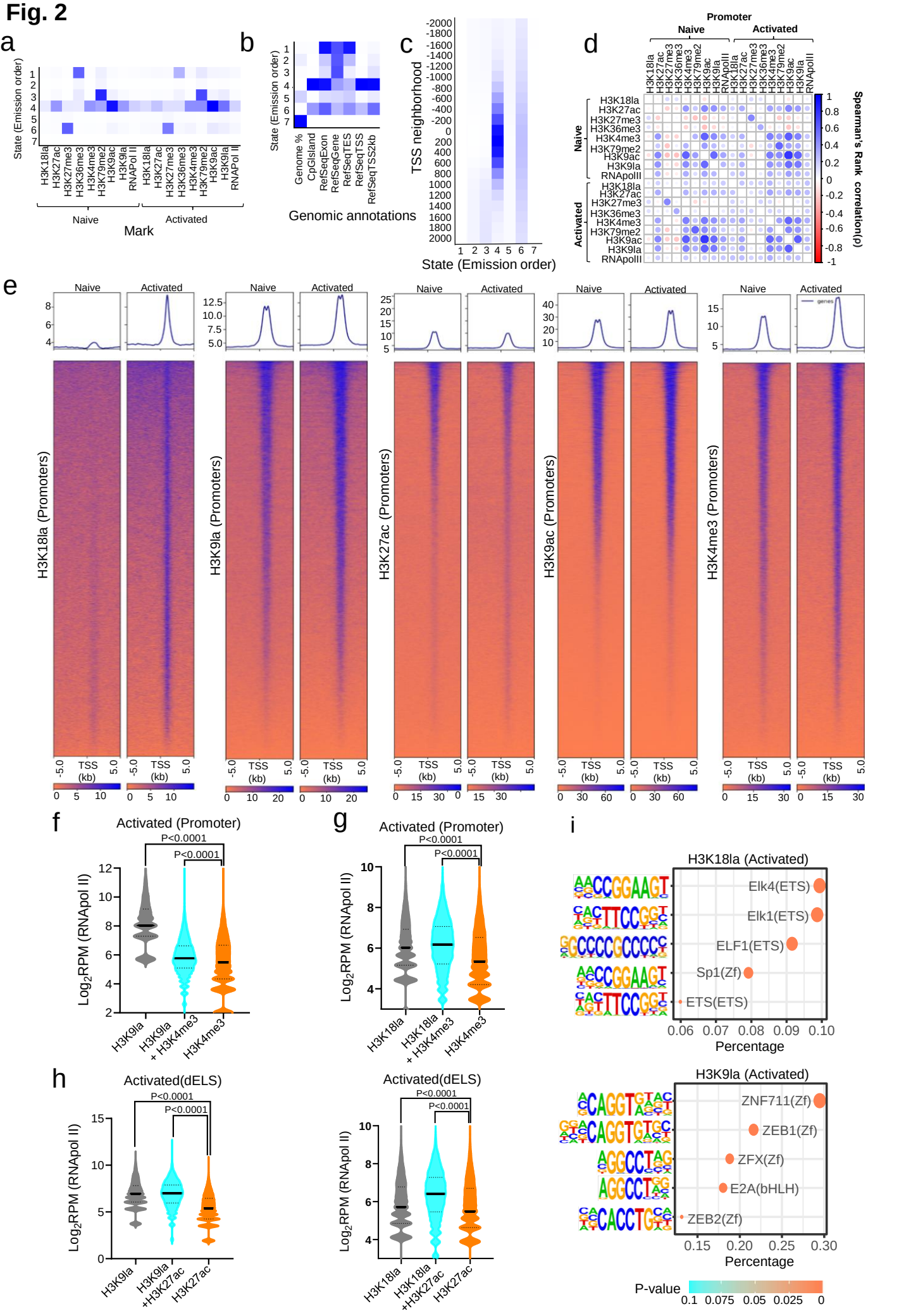
a
State (Emission order)
H3K18la
H3K27ac
H3K27me3
H3K36me3
H3K4me3
H3K79me2
H3K9ac
H3K9la
RNAPol II
Naive
Activated
Mark
b
State (Emission order)
Genome %
CpGIsland
RefSeqExon
RefSeqGene
RefSeqTES
RefSeqTSS
RefSeqTSS2kb
Genomic annotations
c
TSS neighborhood
State (Emission order)
d
Promoter
Naive
Activated
Spearman's Rank correlation(ρ)
e
Naive
Activated
H3K18la (Promoters)
H3K9la (Promoters)
H3K27ac (Promoters)
H3K9ac (Promoters)
H3K4me3 (Promoters)
TSS (kb)
f
Activated (Promoter)
P<0.0001
Log2RPM (RNApol II)
H3K9la
H3K9la + H3K4me3
H3K4me3
g
Activated (Promoter)
H3K18la
H3K18la + H3K4me3
H3K4me3
i
H3K18la (Activated)
Elk4(ETS)
Elk1(ETS)
ELF1(ETS)
Sp1(Zf)
ETS(ETS)
Percentage
H3K9la (Activated)
ZNF711(Zf)
ZEB1(Zf)
ZFX(Zf)
E2A(bHLH)
ZEB2(Zf)
P-value
h
Activated(dELS)
H3K9la
H3K9la +H3K27ac
H3K27ac
H3K18la
H3K18la +H3K27ac

Fig. 3

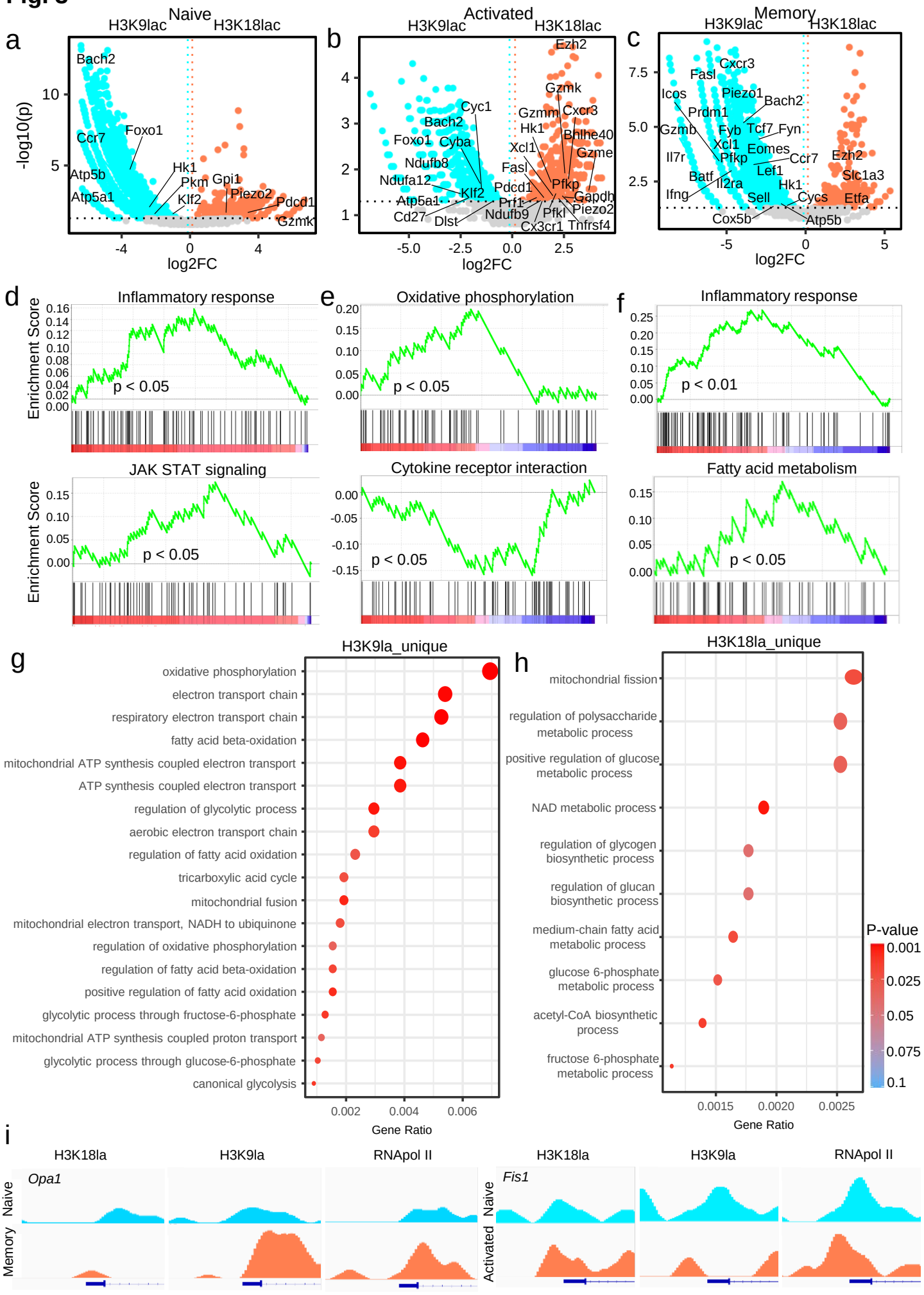
a
Naive
H3K9lac
H3K18lac
-log10(p)
log2FC
Bach2
Foxo1
Ccr7
Hk1
Pkm
Gpi1
Atp5b
Atp5a1
Klf2
Piezo2
Pdcd1
Gzmk
b
Activated
Ezh2
Gzmk
Cyc1
Gzmm
Cxcr3
Bach2
Hk1
Bhlhe40
Foxo1
Cyba
Xcl1
Gzme
Ndufb8
Fasl
Ndufa12
Pdcd1
Pfkp
Klf2
Gapdh
Atp5a1
Prf1
Piezo2
Cd27
Dlst
Ndufb9
Pfkl
Cx3cr1
Tnfrsf4
c
Memory
Cxcr3
Fasl
Icos
Piezo1
Bach2
Prdm1
Gzmb
Fyb
Tcf7
Fyn
Xcl1
Eomes
Il7r
Pfkp
Ccr7
Ezh2
Lef1
Batf
Il2ra
Hk1
Slc1a3
Ifng
Sell
Cycs
Etfa
Cox5b
Atp5b
d
Inflammatory response
Enrichment Score
p < 0.05
e
Oxidative phosphorylation
p < 0.05
f
Inflammatory response
p < 0.01
JAK STAT signaling
p < 0.05
Cytokine receptor interaction
p < 0.05
Fatty acid metabolism
p < 0.05
g
H3K9la_unique
oxidative phosphorylation
electron transport chain
respiratory electron transport chain
fatty acid beta-oxidation
mitochondrial ATP synthesis coupled electron transport
ATP synthesis coupled electron transport
regulation of glycolytic process
aerobic electron transport chain
regulation of fatty acid oxidation
tricarboxylic acid cycle
mitochondrial fusion
mitochondrial electron transport, NADH to ubiquinone
regulation of oxidative phosphorylation
regulation of fatty acid beta-oxidation
positive regulation of fatty acid oxidation
glycolytic process through fructose-6-phosphate
mitochondrial ATP synthesis coupled proton transport
glycolytic process through glucose-6-phosphate
canonical glycolysis
Gene Ratio
h
H3K18la_unique
mitochondrial fission
regulation of polysaccharide metabolic process
positive regulation of glucose metabolic process
NAD metabolic process
regulation of glycogen biosynthetic process
regulation of glucan biosynthetic process
medium-chain fatty acid metabolic process
glucose 6-phosphate metabolic process
acetyl-CoA biosynthetic process
fructose 6-phosphate metabolic process
Gene Ratio
P-value
i
H3K18la
H3K9la
RNApol II
Opa1
Naive
Memory
Fis1
Activated

Fig. 4

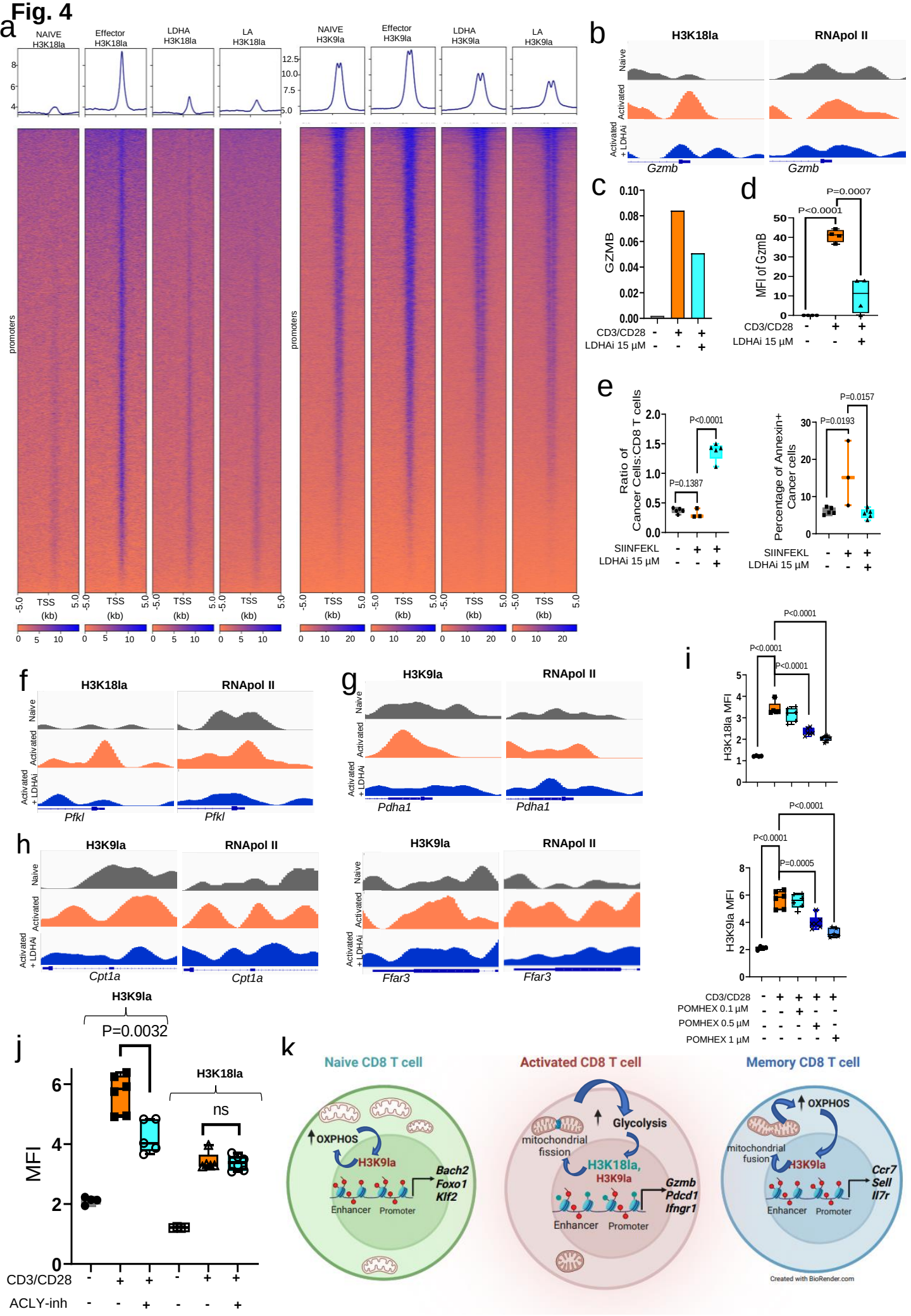
a
NAIVE H3K18la
Effector H3K18la
LDHA H3K18la
LA H3K18la
NAIVE H3K9la
Effector H3K9la
LDHA H3K9la
LA H3K9la
promoters
TSS (kb)
b
H3K18la
RNApol II
Naive
Activated
Activated + LDHAi
Gzmb
c
GZMB
CD3/CD28
LDHAi 15 μM
d
MFI of GzmB
P=0.0007
P<0.0001
e
Ratio of Cancer Cells:CD8 T cells
P<0.0001
P=0.1387
Percentage of Annexin+ Cancer cells
P=0.0157
P=0.0193
SIINFEKL
f
Pfkl
g
H3K9la
Pdha1
h
Cpt1a
Ffar3
i
H3K18la MFI
H3K9la MFI
P<0.0001
P=0.0005
POMHEX 0.1 μM
POMHEX 0.5 μM
POMHEX 1 μM
j
MFI
P=0.0032
ns
ACLY-inh
k
Naive CD8 T cell
Activated CD8 T cell
Memory CD8 T cell
OXPHOS
Glycolysis
mitochondrial fission
mitochondrial fusion
Enhancer
Promoter
Bach2
Foxo1
Klf2
Gzmb
Pdcd1
Ifngr1
Ccr7
Sell
Il7r
Created with BioRender.com

Extended Data Fig. 1

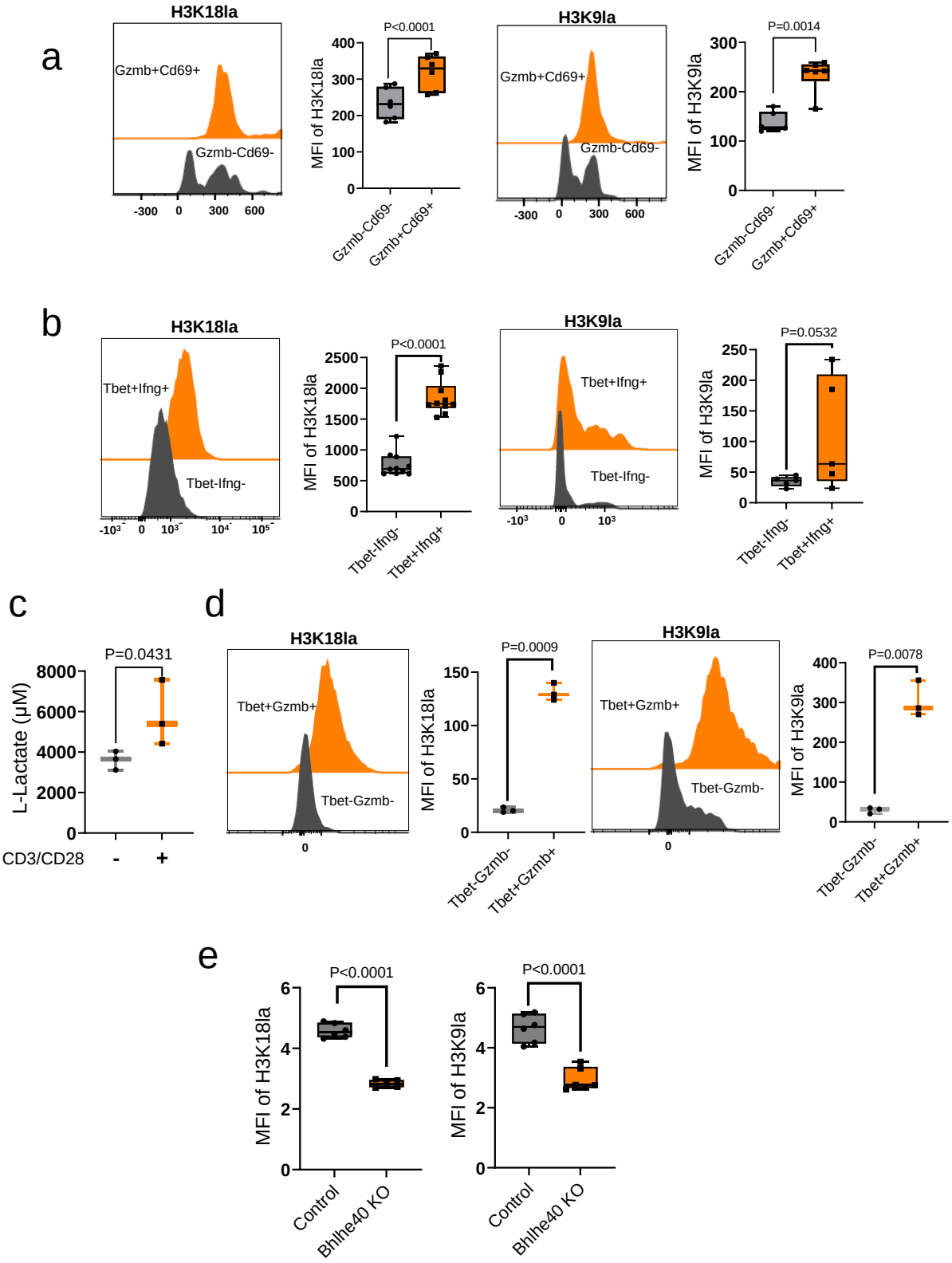

Extended Data Fig. 2

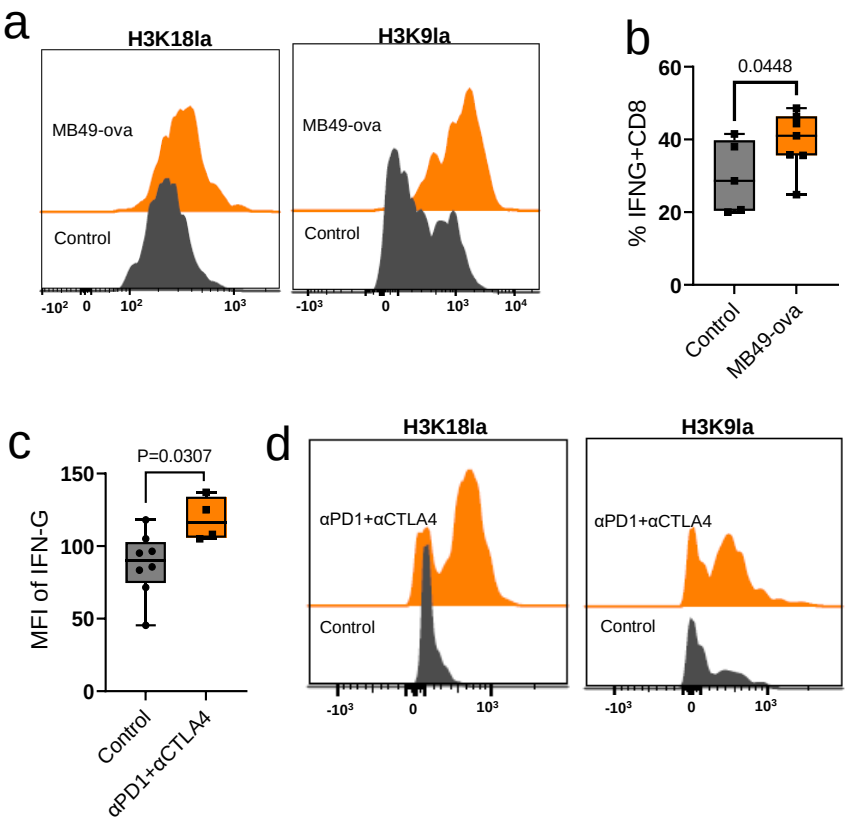

Extended Data Fig. 3

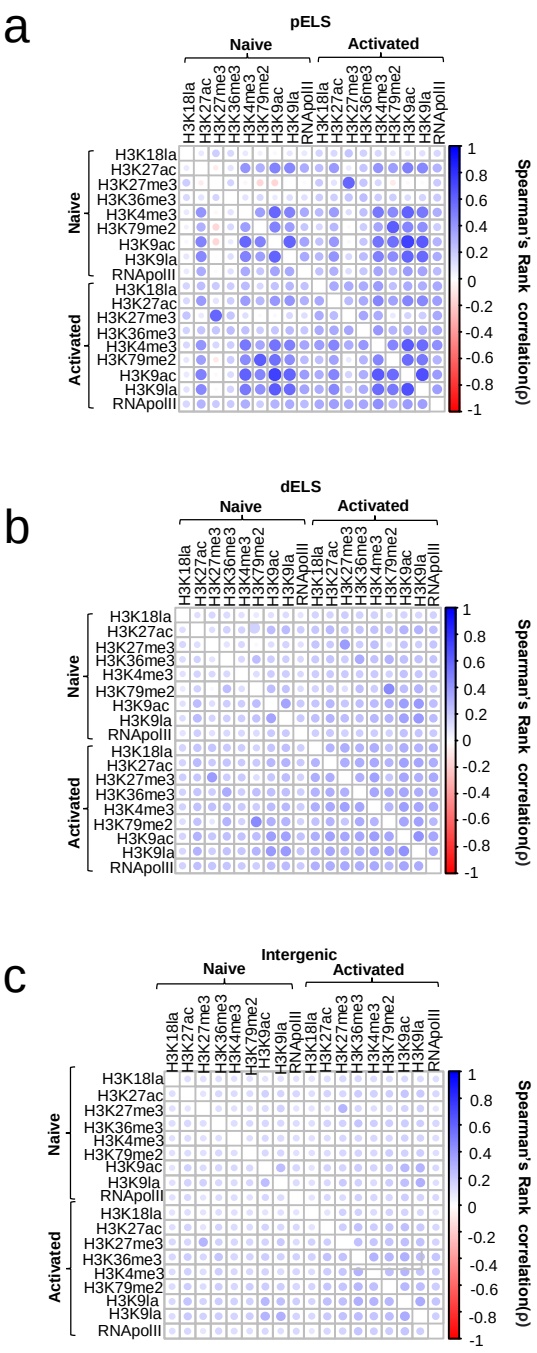

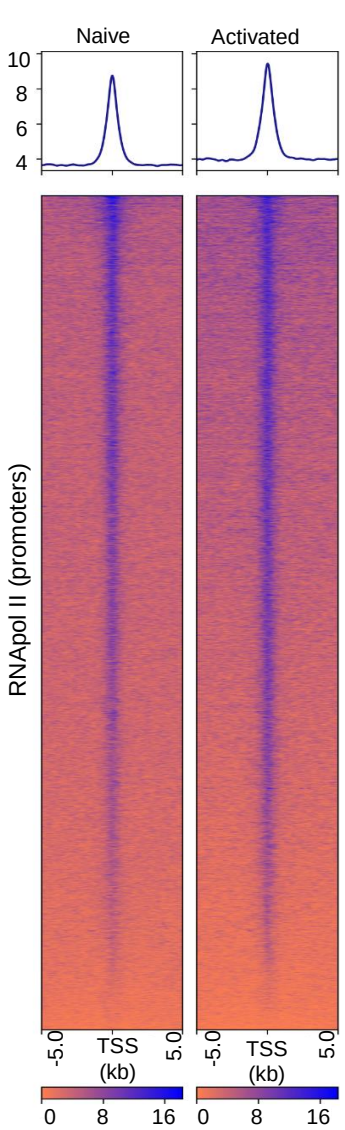

Extended Data Fig. 4

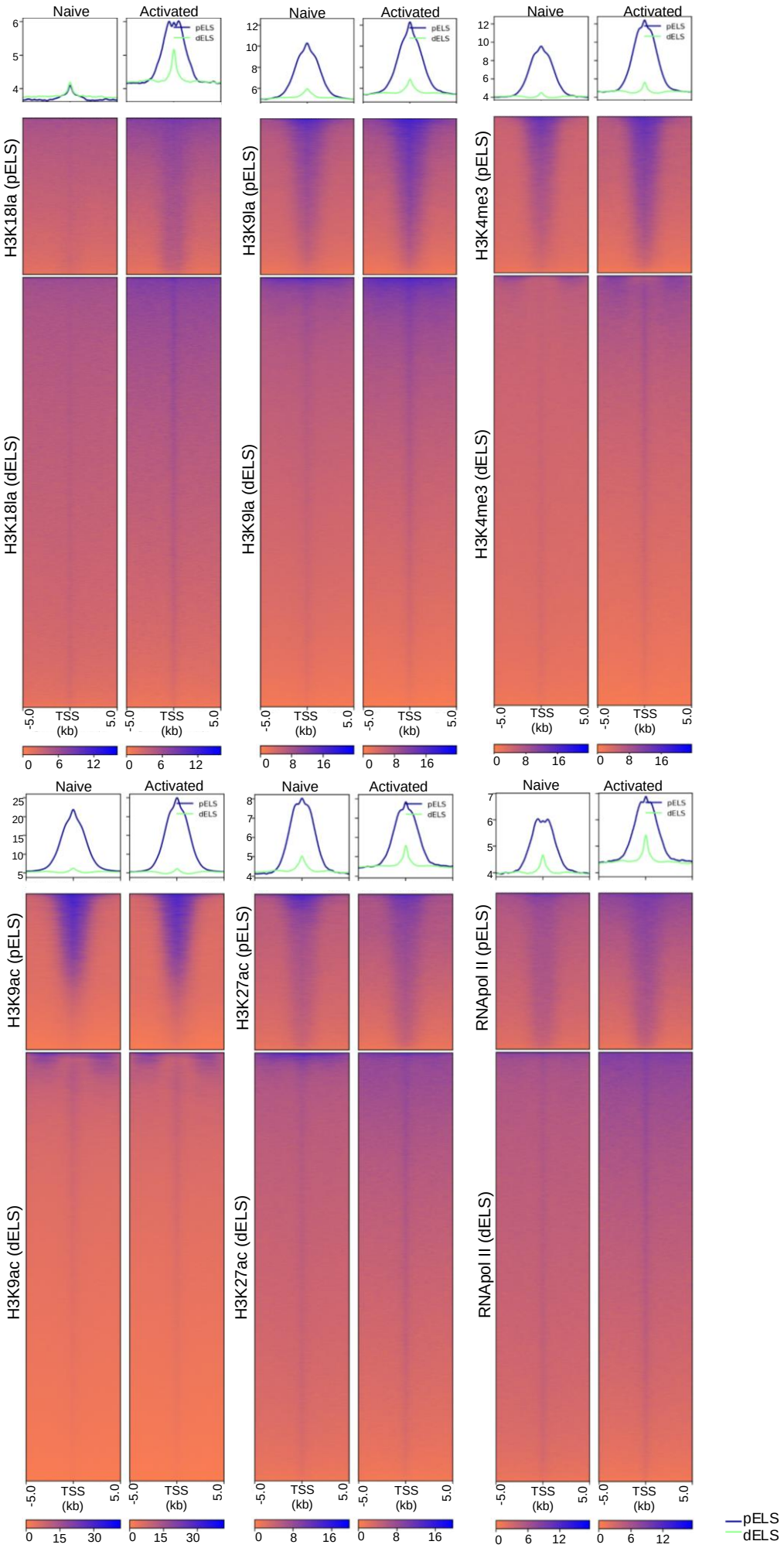

Extended Data Fig. 5

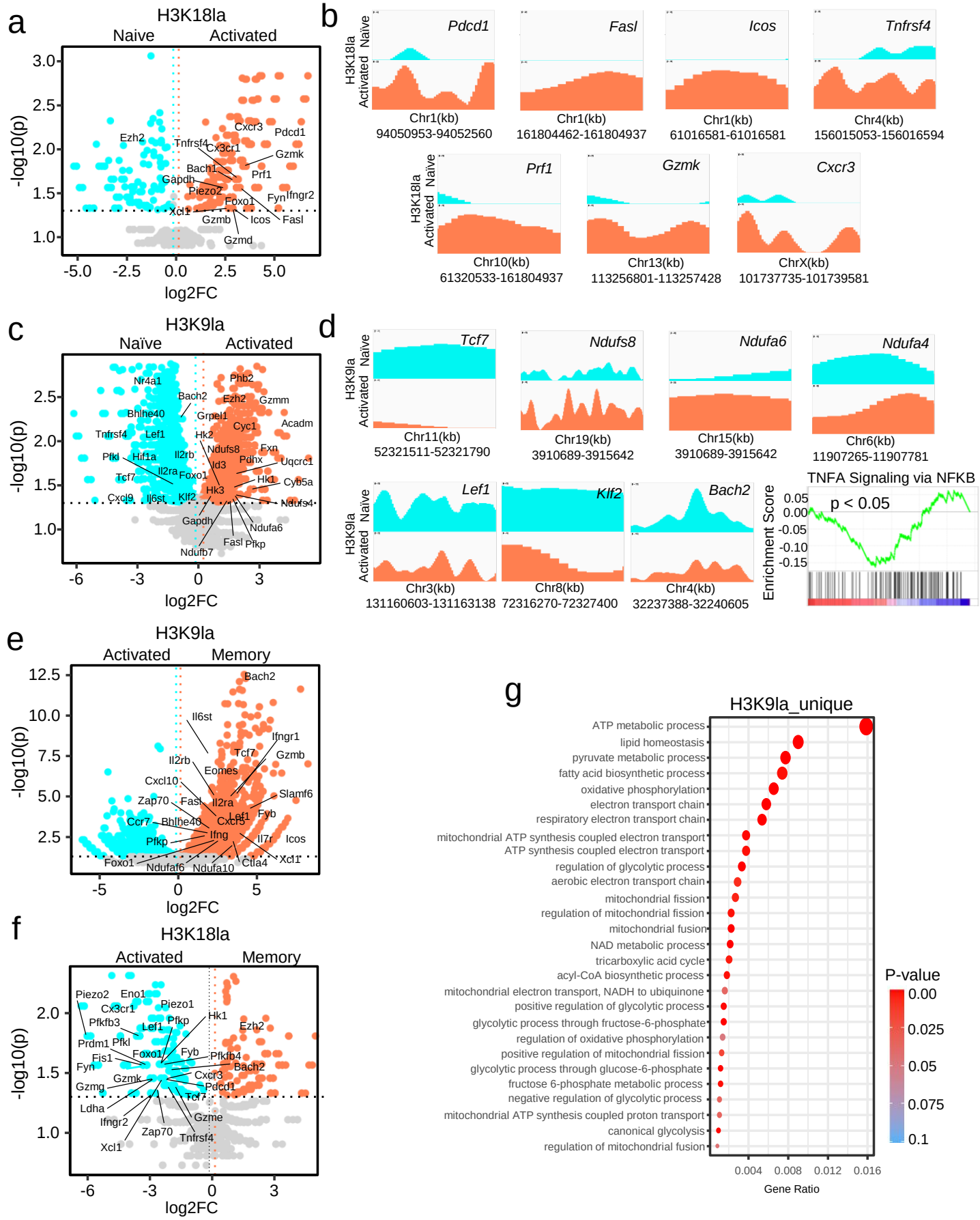

Extended Data Fig. 6

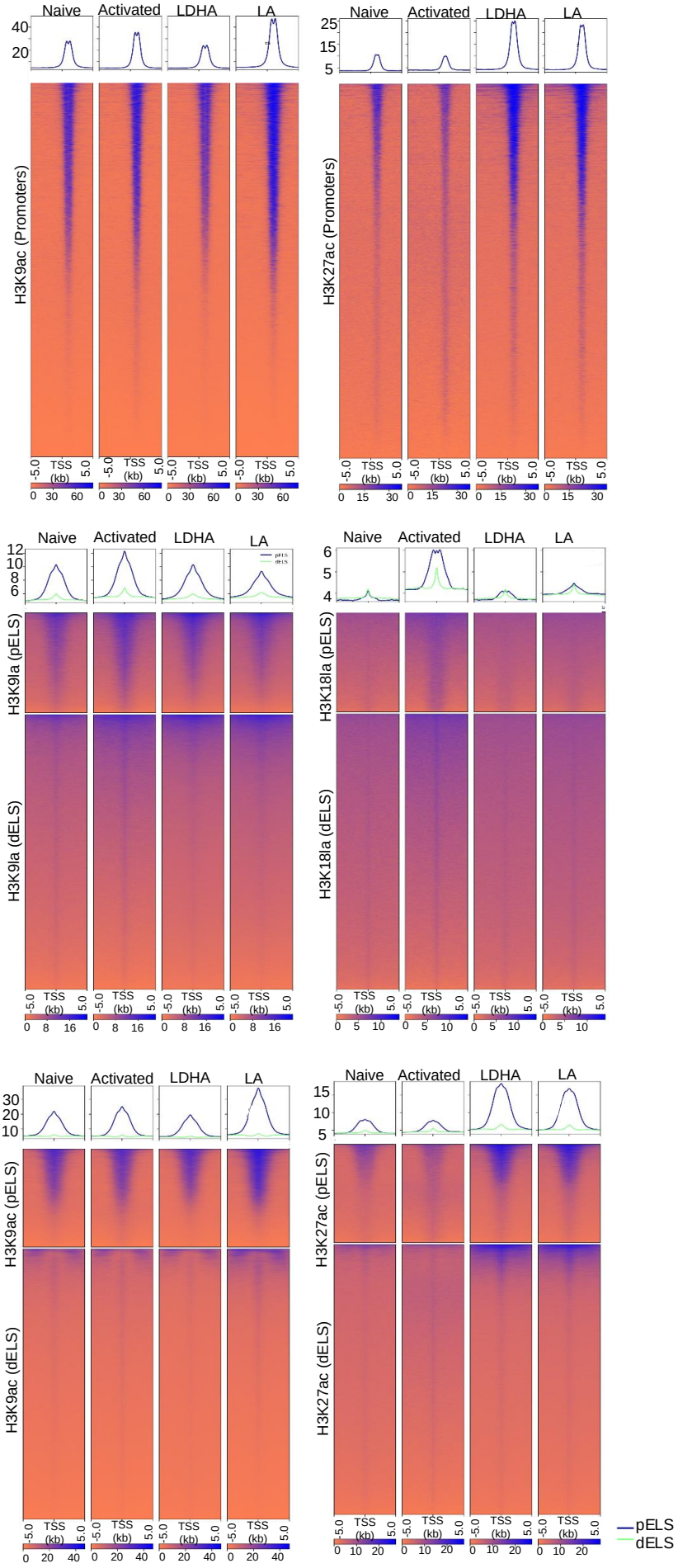

Extended Data Fig. 7

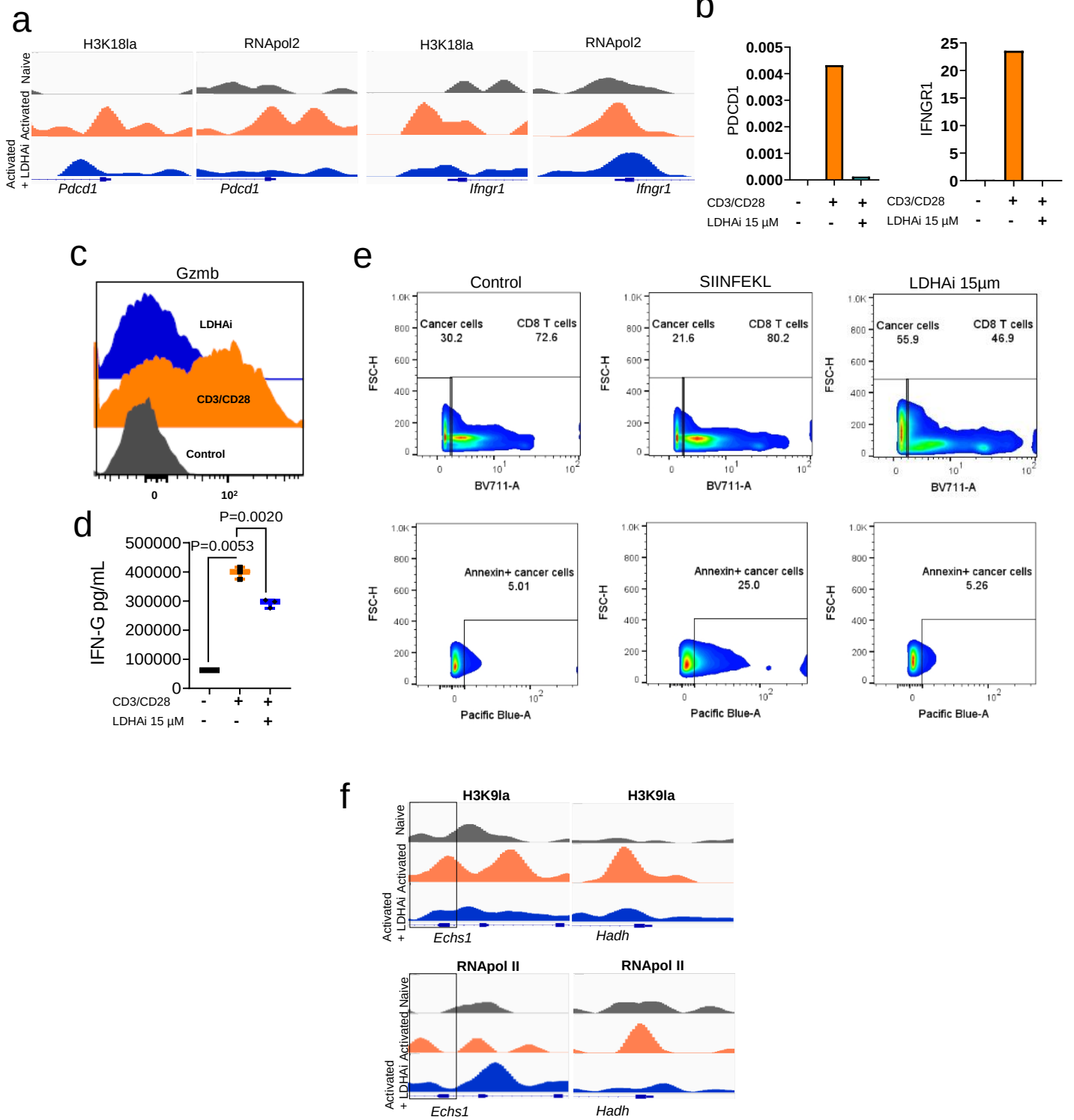

Extended Data Fig. 8

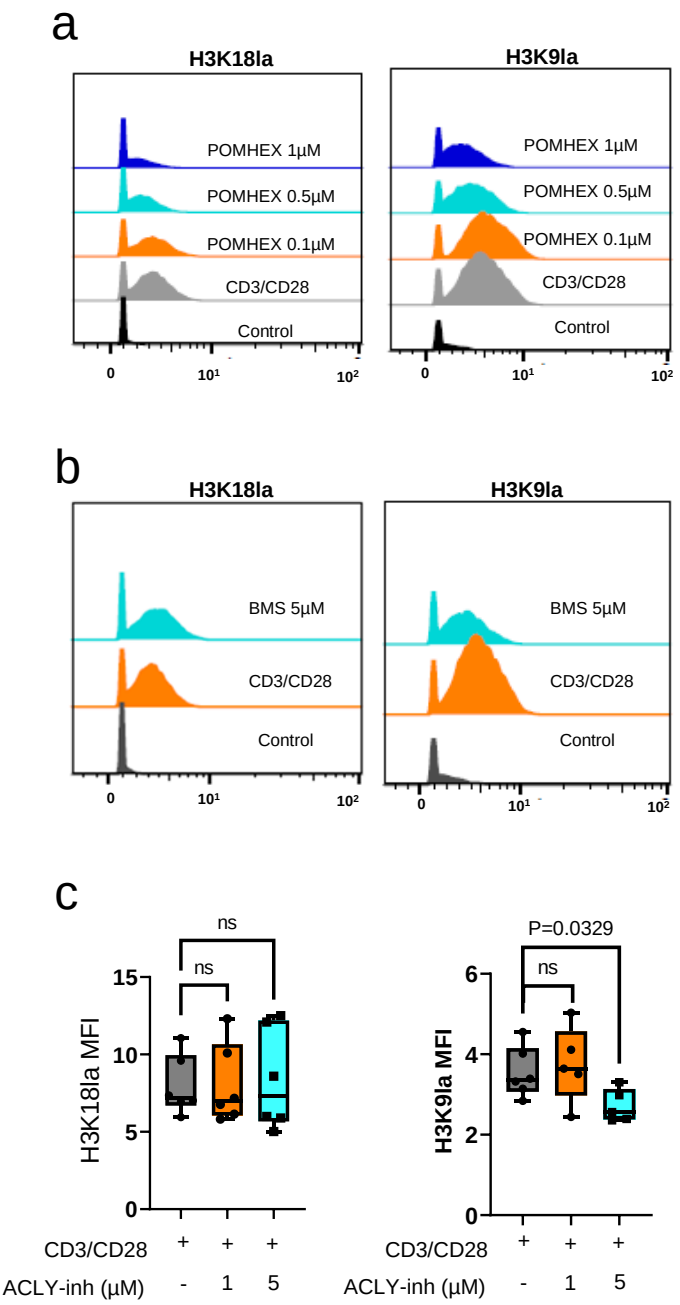

Supplementary Table 1: Key Resource table with list of antibodies

ChIP antibodies

Marker	Clone	Company	Catalog number	Dilution
H3K18LA	22h2L3	PTM-Bio	Cat#PTM-1406RM	10ug per pull down reaction
H3K9LA	13H2L1	PTM-Bio	Cat#PTM-1419RM	10ug per pull down reaction
RNA POL II	4H8	Active Motif	Cat#39097	10ug per pull down reaction
H3K4ME3		Active Motif	Cat#39159	10ug per pull down reaction
H3K9AC		Active Motif	Cat#39137	10ug per pull down reaction
H3K27AC		Active Motif	Cat#39133	10ug per pull down reaction
H3K79ME2		Active Motif	Cat#39143	10ug per pull down reaction
H3K36ME3		Active Motif	Cat#61021	10ug per pull down reaction
H3K27ME3		Active Motif	Cat#39155	10ug per pull down reaction

Flow antibodies

Marker	Clone	Company	Catalog number	Dilution
Annexin V Pacific Blue		ThermoFisher Scientific	Cat # A35122	1:10
Live/ Dead Pacific Orange		Invitrogen	Cat # L34968	1:500
Anti-CD45 AF532, Mouse	30-F11	Invitrogen eBioscience	Cat # 58-0451-82	1:50
Anti-CD3e FITC, Mouse	17A2	Invitrogen eBioscience	Cat # 11-0032-82	1:50
Anti-CD8 BV711, Mouse	53-6.7	BD Biosciences	Cat # 563046	1:50
Anti-H3K18lac AF647	22h2L3	PTM-BIO	Cat # PTM-1406RM	1:100
Anti-H3K9lac AF647	13H2L1	PTM-BIO	Cat # PTM-1419RM	1:100
Anti-GzmB PB, Mouse	GB11	Biolegend	Cat # 515408	1:25
Anti-GzmB BV421, Mouse	QA18A28	Biolegend	Cat # 396414	1:25
Anti-Tbet PerCPCy5.5, Mouse	eBio4B10	Invitrogen eBioscience	Cat # 45-5825-82	1:25
Anti-IFN-G PEeFluor610, Mouse	XMG1.2	Invitrogen eBioscience	Cat # 61-7311-82	1:25
Anti-CD3 FITC, Human	OKT3	Biolegend	Cat # 317306	1:50
Anti-CD8 BV711, Human	SK1	Biolegend	Cat # 344734	1:50
Anti-CD69 PerCPCy5.5, Human	FN50	Biolegend	Cat # 310926	1:50
Anti-GzmB BV421, Human	QA18A28	Biolegend	Cat # 396414	1:25

Other reagents

Reagent	Company	Catalog number
Permeabilization buffer	Invitrogen	Cat # 00-8333-56
Fixation/Permeabilization Diluent	eBioscience	Cat # 00-5223-56
Fixation/Permeabilization Concentrate	eBioscience	Cat # 00-5123-43
Murine IL-2	Peprotech	Cat # 212-12
Murine IL-15	Biolegend	Cat # 566302
LS Columns	Miltenyi Biotec	Cat # 130-042-401
High Sensitivity DNA kit	Agilent	Cat # 5067- 4626
AF647 Labeling Kit	ThermoFisher	Cat # A20186
Liberase TL	Roche	Cat # 5401020001
Dnase I	Roche	Cat # 9003-98-9
ACK Lysis Buffer	Life Technologies	Cat # A1049201
Anti-mouse CD3e Clone: 145-2C11	BD Biosciences	Cat # 553057
Anti-mouse CD28 Clone: 37.51	BD Biosciences	Cat # 553294
SYBR Green Powerup Mastermix	ThermoFisher	Cat # A25742
Purifilied Mouse Anti-Human CD3	BD Pharmigen	Cat # 555336
Purifilied Mouse Anti-Human CD28	BD Pharmigen	Cat # 556620
TriZol reagent	Invitrogen	Cat # 15596026
Superscript III cDNA kit	Invitrogen	Cat # 4368814
GSK2837808A (LDHA Inhibitor)	MedChemExpress	Cat # HY-100681
SIINFEKL Peptide	AnaSpec	Cat # AS-60193-5
GP-100 Peptide	AnaSpec	Cat # AS- 64752
LCMV Peptide	AnaSpec	Cat # AS-61669
Sodium L-Lactate	Sigma Aldrich	Cat # L7022
MAGnify™ Chromatin Immunoprecipitation System	Applied Biosystems	Cat # 492024
dsDNA HS Assay kit	Invitrogen	Cat # Q32851
Phosphatase Inhibitor Cocktail	Active Motif	Cat # 37493
POMHEX Enolase Inhibitor	MedChemExpress	Cat # HY-131904
Chloroform	Sigma Aldrich	Cat # C2432
Isopropanol	Sigma Aldrich	Cat # 19516
BMS-303141	MedChemExpress	Cat # HY-16107
ELISA MAX™ Standard Set Mouse IFN-G	Biolegend	Cat # 430801
TMB Substrate Solution Set	Biolegend	Cat # 421101
Stop Solution	Biolegend	Cat # 423001
ELISA Assay Diluent (5X)	Biolegend	Cat # 421203
ELISA Wash Buffer (20X)	Biolegend	Cat # 421601
ELISA Coating Buffer	Biolegend	Cat # 421701
L-Lactate Assay Kit	Cayman Chemicals	Cat # 700510
Naive CD8a+ T Cell Isolation Kit, Mouse	Miltenyi Biotec	Cat # 130-096-543
CellTrace Violet	Invitrogen	Cat # C34571
Anti-CTLA4 Clone:9H10	Bio X Cell	Cat # BE0131
Anti-PD1 Clone:RMP1-14	Bio X Cell	Cat # BE0146

Mouse lines

Mouse line	Company	Catalog number	Age
C57BL/6	NCI	556 C57BL/6NCr	5-7 weeks old
OT-I	Jackson Laboratory	0003831 C57BL/6-Tg(TcraTcrb)1100Mjb/J	5-7 weeks old
Pmel	Jackson Laboratory	005023 B6. Cg- Thy1a/Cy Tg(TcraTcrb)8Rest/J	5-7 weeks old
Bhlhe40 KO	Jackson Laboratory	029732 B6.129S1 (Cg)-Bhlhe40 tm1.1 Rhli/MpmJ	5-7 weeks old

Primer

Primer name	Sequence
MuBetaactin Forward	5'- CCACTGTCGAGTCGCGTCCA -3'
MuBetaactin Reverse	5'- CACCATCACACCCTGGTGCC -3'
MuIfngr1 Forward	5'- CTCGGTGCCTGTACCGACGA -3'
MuIfngr1 Reverse	5'- GGGGCCCGACCTTTCCCTTT -3'
MuGzmb Forward	5'- TCCAGGACAAAGGCAGGGGAGA -3'
MuGzmb Reverse	5'- TGTGGGCCCCCAAAGTGACAT -3'
MuPdcd1 Forward	5'- GCAAGGACGACACTCTGAAGGAGG -3'
MuPdcd1 Reverse	5'- CCCCTACGTCCCATGGCCGA -3'

Software

Data analysis softwares	FlowJo V10 (Tree Star, Ashland, OR), ggplot2 v3.4.2, MACS2 v2.2.8, FastQC v0.11.9, bowtie2 v2.3.5.1, SAMBLASTER v0.1.26, SAMTOOLS v1.13, SAMBAMBA v0.6.6, CHIPseeker v1.30.3, clusterProfiler v4.2.2,ChIPpeakAnno v3.28.1, MAnorm v1.3.0, deepTools v3.5.1, IGV v2.16.0,EdgeR v3.36.0, Homer v4.11.1,GraphPad Prism software v9, R v4.0.2, Rstudio v4.1.2